Title
Excitation functions and mass asymmetric fission barriers for compound nuclei 70,76Se

Journal
Nuclear Physics A, 679(2)

Author
Fan, T.S.

Publication Date
2000-05-01

LBNL-45730
Preprint

ERNEST ORLANDO LAWRENCE
BERKELEY NATIONAL LABORATORY

Excitation Functions and Mass Asymmetric Fission Barriers for Compound Nuclei ^{70,76}Se

T.S. Fan, K.X. Jing, L. Phair, K. Tso, M. McMahan,
K. Hanold, G.J. Wozniak, and L.G. Moretto

Nuclear Science Division

May 2000

Submitted to
Nuclear Physics A

DISCLAIMER

LBNL-45730

Excitation Functions and Mass Asymmetric Fission Barriers for Compound Nuclei ^{70,76}Se

T.S. Fan,[1] K.X. Jing,[4] L. Phair,[4] K. Tso,[2] M. McMahan,[4]
K. Hanold,[3] G.J. Wozniak,[4] and L.G. Moretto[4]

[1]Institute for Heavy Ion Physics
Department of Technical Physics
Peking University
Beijing 100871, China

[2]Look Ease Enterprises Ltd.
Dominion Centre, 43-45, Queen's Road East
Hong Kong

[3]Syagen Technology
1411 Warren Avenue
Tustin, California 92780

[4]Nuclear Science Division
Ernest Orlando Lawrence Berkeley National Laboratory
University of California
Berkeley, California 94720

May 2000

This work was supported by the Director, Office of Science, Office of High Energy and Nuclear Physics, Division of High Energy Physics, of the U.S. Department of Energy under Contract No. DE-AC03-76SF00098.

Excitation Functions and Mass Asymmetric Fission Barriers for Compound Nuclei ^{70,76}Se

T.S. Fan[1†], K.X. Jing, L. Phair, K. Tso[2], M. McMahan,
K. Hanold[3], G.J. Wozniak, and L.G. Moretto
Nuclear Science Division, Lawrence Berkeley National Laboratory,
University of California, Berkeley, California 94720

(Dated: May 18, 2000)

Abstract

Excitation functions were measured for complex fragments with atomic number Z = 5-20 emitted from the compound nuclei ^{70,76}Se produced in the reactions ^{58,64}Ni + ^{12}C. Mass asymmetric fission barriers were extracted by fitting the excitation functions with a transition state formalism. The extracted barriers were compared with those calculated from macroscopic nuclear models. The measured barriers for symmetric fission seem to support the hypothesis of a shape-dependent congruence energy, which doubles for fission of strongly indented saddle-point shapes. All of the measured excitation functions can be scaled onto a single straight line according to the transition state prediction.

PACS number(s): 24.60.Dr, 25.85.Ge, 24.75.+i, 25.85.Ge

KEYWORDS: nuclear reactions ^{12}C(^{58,64}Ni,X), E = 6-14 AMeV; measured $\sigma(Z)$ vs E; deduced mass asymmetric fission barriers for ^{70,76}Se; transition state fission rates.

†The corresponding author. Address: MS 88, Lawrence Berkeley National Laboratory, Berkeley, CA 94720, USA. Phone: (510)486-7961. Fax: (510)486-7983. Email: TSFan@lbl.gov

I. INTRODUCTION

The emission of complex fragments from a compound nucleus can be considered as a form of asymmetric fission controlled by mass-asymmetry dependent barriers (B_Z) [1–4]. The decay width Γ_Z for emitting a complex fragment of charge Z is determined by the barrier B_Z for each binary division and by the nuclear temperature T_Z at the barrier, and has the approximate form $\Gamma_Z \propto \exp(-B_Z/T_Z)$ [4]. The mass asymmetric fission barriers (or conditional barriers) represent the height of the ridge-line in the potential energy surface defined as the locus of the conditional saddle points as a function of mass asymmetry (or Z). The dependence of the conditional barriers on the asymmetry of the binary division determines the charge or mass distributions of the emitted fragments [4]. For a light compound nucleus below the Businaro-Gallone point [5], there is no longer a traditional fission saddle point. The ridge line rises monotonically towards symmetry. The disappearance of a stable symmetric saddle leads to the disappearance of fission as a process distinct from evaporation. Thus the mass distributions of the complex fragments are "U" shaped with a minimum corresponding to symmetric division[6, 7]. The determination of the precise dependence of conditional barriers upon mass asymmetry requires the measurement of the entire mass distribution at various bombarding energies. It is difficult to perform these measurements in light systems because of the low yield for symmetric decay at the typically low excitation energies of the compound nucleus. Up to now, only four nearly complete sets of experimental mass asymmetric fission barriers have been measured for the compound nuclei ^{75}Br [6] and ^{90,94,98}Mo [7], and a partial set for ^{110,112}In[8].

Mass asymmetric fission barriers can be calculated with macroscopic nuclear models. It has been claimed that the Rotating Finite-Range Model (RFRM) [9, 10] reproduces the zero-angular momentum mass-asymmetric fission barriers for two of the previously measured compound nucleus systems ^{75}Br [6] and ^{110,112}In [8]. In recent work, Jing *et al.* [7] measured the excitation functions for complex fragments with atomic number Z = 5-25 emitted from the compound nucleus isotopes ^{90,94,98}Mo produced in the ^{78,82,86}Kr + ^{12}C reactions. The

mass asymmetric fission barriers extracted from the excitation functions, however, lie between the calculations of the RFRM and the Rotating Liquid Drop Model (RLDM). Boger and Alexander [11] have also reported similar results for the reaction ^{86}Kr + ^{63}Cu. To assess the significance of this disagreement with the current macroscopic models, additional data are necessary. The study of additional light nuclei (A<100) is desirable in particular, since in this mass region the mass asymmetric barriers for the RFRM and RLDM models differ by as much as 10 MeV [6].

In recent papers[12–14, 7], the excitation functions for the symmetric fission of heavy nuclei and the asymmetric fission of medium mass nuclei were shown to scale exactly according to transition state predictions. In the present work we extend the test of this scaling to the light medium mass region.

In this work, complex fragment emission from compound nuclei ^{70}Se and ^{76}Se, representing neutron-poor (n/p = 1.06) and neutron-rich (n/p = 1.24) nuclei of atomic number Z = 34, has been studied. Excitation functions have been obtained for complex fragments with Z = 5-20 emitted from ^{70}Se produced in the ^{58}Ni + ^{12}C reactions at eight bombarding energies (E = 6.07, 7.03, 8.07, 9.17, 10.35, 11.59, 12.91, 14.29 AMeV), and for those emitted from ^{76}Se produced in the ^{64}Ni + ^{12}C reactions at six bombarding energies (E = 6.63, 7.54, 8.51, 9.53, 10.62, 12.95 AMeV). Two nearly complete sets of mass asymmetric fission barriers have been extracted by fitting the measured excitation functions with a transition state formalism, following the procedure in ref. [7]. In addition, a new global fitting method is utilized to allow barrier extraction with improved systematic consistency.

The outline of the paper follows. The experimental methods are detailed in Section II. The experimental results obtained from inclusive and coincidence measurements are presented in Section III. In Section IV, the procedure used to extract the mass asymmetric fission barriers and the extracted barriers are presented and compared to several macroscopic models. In Section V, the measured excitation functions for these two compound nuclei are shown to scale exactly according to the transition state predictions. The summary and conclusions are contained in Section VI.

II. EXPERIMENTAL PROCEDURE

The measurements were carried out at the 88-Inch Cyclotron of the Lawrence Berkeley National Laboratory. An Advanced Electron-Cyclotron-Resonance (AECR) ion source[15] was utilized to produce the high charge state ^{58}Ni and ^{64}Ni ions which, after injection into the cyclotron and acceleration to the desired energy, then impinged on a high purity [16] carbon target (1.0 mg/cm^2). The thin target ensured that the projectile's energy loss within the target was modest (about 4.6% of the initial beam energy for the lowest bombarding energy E = 6.07 AMeV).

The complex fragments emitted in the reactions were detected in two position-sensitive $\Delta E - E$ detector assemblies placed on either side of the beam. Each assembly consisted of four $\Delta E - E$ telescopes. Each telescope consisted of a gas ionization ΔE detector followed by a 5 mm thick Li-drifted Si counter, with surface dimensions of 45×45 mm^2, and subtending 5° both in- and out-of-plane. The telescopes were position sensitive in two dimensions and were used to determine the energy, the atomic number, the in-plane and out-of-plane angles for each fragment that traversed the ΔE and stopped in the E detector. The telescopes within each quad assembly were located in a plane, with a separation of 1.6° between the active edges of adjacent telescopes. Thus, a single quad unit covered an angular range of 24.8° in-plane. The in-plane angular range of the two quad units were overlapped to cover the gaps between the adjacent telescopes. In this way, fairly complete and continuous angular distributions were obtained using only a relatively small amount of beam time.

The methods of the energy and position calibrations of the ΔE and E detectors have been described previously in refs. [7, 17]. The energy calibrations were performed by directly exposing the detectors to low intensity "cocktail" beams, composed of ions with similar mass-to-charge ratios: $^{17}O^{5+}$, $^{24}Mg^{7+}$, $^{34}S^{10+}$, $^{48}Ti^{14+}$, $^{65}Cu^{19+}$ (10.4 AMeV), and $^{21}Ne^{7+}$, $^{24}Mg^{8+}$, $^{27}Al^{9+}$, $^{30}Si^{10+}$, $^{36}S^{12+}$, $^{39}K^{13+}$ (13.3 AMeV). The in-plane position was self-calibrated [18]. The out-of-plane position was calibrated with a mask which could be lowered into position remotely. The energy calibrations are accurate to ±1%, and the position resolution obtained

was $\pm 0.2°$. The beam charge collected in a Faraday cup was used to determine the cross sections. The charge state of the ^{58}Ni or ^{64}Ni ions entering the Faraday cup was determined from the systematics of McMahan [19]. Inclusive and coincidence events were recorded on magnetic tape and analyzed off-line.

III. EXPERIMENTAL RESULTS

A Velocity Plots

To identify the source of the complex fragments, the laboratory energy spectra were transformed into cross section plots $\partial^2\sigma/\partial V_{\|}\partial V_{\perp}$ in velocity space. The velocity for each detected fragment was evaluated from its measured energy and atomic number using the mass parameterization of ref. [20]: $A = 2.08Z + 0.0029Z^2$. This formula predicts the average mass number of the fragment with an accuracy of ± 0.5 atomic mass units for Z-values between $5 \leq Z \leq 40$. Only fragments with $4 < Z < 21$ were considered in this analysis. Fig. 1 shows linear contour plots of the cross section $\partial^2\sigma/\partial V_{\|}\partial V_{\perp}$ in the $V_{\|} - V_{\perp}$ plane for representative Z-species detected in the ^{64}Ni + ^{12}C reaction at bombarding energy $E = 9.53$ AMeV. In Fig. 2, some examples of contour plots are shown for the ^{58}Ni+^{12}C reaction at four different bombarding energies. For all Z-values, these plots show the presence of an "isotropic" component (isotropic Coulomb ring, or $d\sigma/d\theta_{c.m.}$=constant) associated with binary compound nucleus emission in the center-of-mass. For lighter fragments ($Z<10$) one can also see the strong target-like deep-inelastic component, which is backward peaked in these reverse kinematics reactions. The centers of the Coulomb rings correspond to the velocity of the source (compound nucleus or composite system) from which the fragments were emitted, and the radii correspond to the emission velocities of the fragments in the source frame. The emission velocity of each fragment is determined mainly by the Coulomb repulsion between the fragment and its partner. The monotonically decreasing emission velocity with increasing fragment Z-value, due to momentum conservation in the source frame, is

reflected in the decreasing size of the Coulomb rings with increasing Z-values (see Figs. 1 and 2). The widths of the rings arise from fluctuations in the Coulomb energy, sequential evaporation of light particles from the primary fragments, fluctuations in the souce velocity, and the presence of different isotopes for a given Z-value.

The degree of target-projectile fusion associated with the reaction producing complex fragments can be inferred from the source velocities, which are smallest for complete fusion and become larger if fewer target nucleons fuse with the projectile. The source velocities for the ^{58}Ni + ^{12}C reactions at different bombarding energies have been determined from the position of the centers of the Coulomb rings for each Z-species, and are plotted as a function of fragment Z-value in the upper portions of each octant of Fig. 3. The data for the ^{64}Ni + ^{12}C reactions present identical features, and are therefore not shown. The single large error bar shown for each data set in Fig. 3 is an estimate of the systematic error associated with the energy calibration, the mass parameterization, and energy losses in the target and in the detector entrance window. The statistical error associated with the source velocity determination is smaller than the size of the symbols used in these figures. The horizontal lines in Fig. 3 represent the expected source velocities for complete fusion reactions, and closely coincide with the experimental source velocities. As expected, these source velocities decrease with decreasing bombarding energy, and at all bombarding energies they are essentially independent of Z, confirming that all fragments are emitted by the same source. For Z-values where the target-like components are present, our inability to separate completely these components from the compound nucleus components may have led to errors in extracting the source velocity and to a slight increase of the source velocity for the lower Z-values seen in Fig. 3.

Also shown in Fig. 3 are the average emission velocities as a function of Z for the ^{58}Ni + ^{12}C reactions. These mean emission velocities display an almost linear decrease with increasing Z, and show very little dependence on the bombarding energy. For comparison, the solid lines show a simple calculation where the emission velocities are calculated solely from the Coulomb repulsion of two fragments after scission. The scission configuration was

assumed to be that of two nearly-touching spheres separated by 2 fm. The Z split for each mass split was calculated assuming charge equilibration. The Coulomb energy was thus estimated as $E_{\rm Coul} = 1.44 Z_1 Z_2/(r_0(A_1^{1/3} + A_2^{1/3}) + 2.0)$ (MeV), where r_0 was determined by equating $E_{\rm Coul}$ for symmetric fission (i.e., $Z_1 = Z_2$, $A_1 = A_2$) to the value given by Viola systematics [21]. The calculated emission velocities agree rather well with the experimental data. The second moments of the experimental velocity distributions $\sigma(V_e)$, i.e., the widths of the Coulomb rings, are also shown in Fig. 3. The second moments appear to be independent of the bombarding energy over the range studied.

B Angular Distributions

Representative examples of the measured angular distributions $d\sigma/d\theta_{c.m.}$ in the reference frame of the source are shown in Fig. 4 for ^{58}Ni + ^{12}C at two bombarding energies. The angular distributions for ^{64}Ni + ^{12}C reactions present identical features, and are therefore not shown. For all Z values and most of the angular range, the isotropic component dominates; it can be identified with the binary decay of the compound nucleus. For the lighter fragments (Z<10) at backward angles, $d\sigma/d\theta_{c.m.}$ increases due to the target-like deep-inelastic products. For fragments with Z>21, the angular distributions were not determined. The fragment Z-values analyzed in this experiment cover the the range of asymmetries Z/Z_{CN} = 0.15 - 0.59 where 0.5 corresponds to symmetric splitting, and Z_{CN} is the compound nucleus atomic number.

C Charge Distributions and Excitation Functions

For the isotropic component of the angular distributions, which is dominant for most fragments, the total cross section for a specific Z-value was determined by extending the average value $d\sigma/d\theta_{c.m.}$ and integrating the extended angular distribution from 0° to 180°. For the non-isotropic distributions of the fragments with Z<10, a constant equal to the

minimum value of $d\sigma/d\theta_{c.m.}$ was taken as the upper limit for the isotropic component, and the cross section was obtained by integrating the constant from 0° to 180°.

The cross sections of the isotropic component, which are of compound nucleus origin, are shown in Figs. 5 and 6 as a function of the fragment Z-values. These cross section data are also tabulated in Tables I and II. All the charge distributions measured for the isotropic components display the characteristic U-shape (or the left side of it) associated with the decay of a compound nucleus below the Businaro-Gallone point. The observed overall flattening of the charge distributions with increasing bombarding energy can be explained by the increase of the nuclear temperature, which tends to make all decay channels more equally probable. Odd-even effects are evident, particularly in the ^{70}Se data. The yields for even Z-species typically are larger than the average trends, and are smaller for odd Z-species. For low excitation energies, shell and pairing effects associated with the saddle-point configuration may give rise to fine structure in the charge distributions. When the excitation energy increases, this fine structure should be progressively washed out due to sequential evaporation and be replaced by fine structure associated with the sequential evaporation itself [22].

Figs. 7 and 8 show the measured excitation functions for the compound nuclei ^{70,76}Se for a series of decay products. All of the excitation functions rise rapidly at low energies, in accordance with the rapid opening up of phase space for complex fragment decay, and then less rapidly at higher energies. This is a characteristic signature of statistical emission from a compound nucleus, observed also in previous works [2, 6, 7].

D Coincidence Data

The binary character of complex fragment emission, clearly shown in the velocity distributions in the source frame (see Fig. 3), can also be seen in the coincidence measurements. Fig. 9 displays, for the ^{58}Ni + ^{12}C reaction, the spectra of $Z_1 + Z_2$ where Z_1 and Z_2 are the charges of the coincident fragments which were detected on the opposite sides of the beam

axis. Essentially, no coincidences between telescopes on the same side of the beam were observed. The numbers to the left of the arrows in the figure indicate the mean total detected charge at the corresponding bombarding energies. The rather sharp peaks located near the total charge (Z_{CN}=34) of the compound nucleus indicate the binary nature of these events. The small difference between Z_{CN} and the mean total detected charge gives the average amount of charged particle evaporation from the hot primary fragments. The average total charge loss at the higher energies is about 4 units and it decreases to about 0.5 units at the lowest bombarding energy.

IV. MASS ASYMMETRIC FISSION BARRIERS

A Extraction procedure

In order to extract the mass-asymmetric fission barriers (or the conditional barriers), the complex-fragment excitation functions have been fit with a function obtained from a transition state formalism [23, 4, 24] for complex fragment decay width Γ_Z, and from the Weisskopf theory [25] for the neutron decay width Γ_n and for the proton decay width Γ_p. The fitting procedure, which has been described in detail in ref. [7], is summarized in the following.

The expression for evaluating the cross section for a given complex fragment of charge Z is given by

$$\sigma_Z = \sum_{\ell=0}^{\ell_{max}} \sigma_\ell \, P_Z(\ell) \,, \tag{1}$$

where σ_ℓ is the cross section for the fusion reaction which produces the compound nucleus of angular momentum $\ell\ \hbar$, and $P_Z(\ell)$ is the probability of emitting a complex fragment of charge Z from a compound nucleus of angular momentum ℓ. In the expression used for $P_Z(\ell)$, we have included second and third chance emissions. The probability for the first chance emission is Γ_Z/Γ_T where the total decay width Γ_T is:

$$\Gamma_T = \Gamma_n + \Gamma_p + \cdots \approx \Gamma_n + \Gamma_p \,, \tag{2}$$

since in this mass region $\Gamma_n + \Gamma_p \gg \sum_{Z>1} \Gamma_Z$. The angular momentum distribution of the fusion cross section was taken to be a triangular distribution, and the total fusion cross section σ_0 thus is:

$$\sigma_0 = \sum_{\ell=0}^{\ell_{\max}} \sigma_\ell = \pi\lambda^2 \sum_{\ell=0}^{\ell_{\max}} (2\ell+1)\, T(\ell), \tag{3}$$

where

$$T(\ell) = \frac{1}{1+\exp((\ell-\ell_{\max})/\delta\ell)}.$$

The quantity $\ell_{\max}$ is the maximum angular momentum. The value of $\delta\ell$, which determines the diffuseness of the distribution, was chosen to be 1, close to that needed to fit experimental fission excitation functions at low bombarding energies [6, 7, 26, 27]. The maximum angular momentum $\ell_{\max}$ can be estimated from theoretical models. In this work, the maximum angular momenta $\ell_{\max}$ were calculated with the Bass Model [28], and were adjusted slightly to minimize the χ^2 of all the fits simultaneously. Both the $\ell_{\max}$ values predicted by the Bass model and those used in the fits are listed in Table III.

The transition state decay width for emission of a complex fragment of charge Z can be expressed as [4]

$$\begin{aligned}\Gamma_Z &= \frac{1}{2\pi\rho(E-E_r^{\rm gs})}\int_0^{E-B_Z-E_r^{\rm s}} \rho^*(E-B_Z-E_r^{\rm s}-\varepsilon)\,d\varepsilon \\ &\approx \frac{T_Z}{2\pi}\,\frac{\rho^*(E-B_Z-E_r^{\rm s})}{\rho(E-E_r^{\rm gs})},\end{aligned} \tag{4}$$

where $\rho(E-E_r^{\rm gs})$ is the level density of the compound nucleus, $\rho^*(E-B_Z-E_r^{\rm s}-\varepsilon)$ is the level density at the conditional saddle with kinetic energy ε in the fission mode; B_Z is the mass-asymmetric fission barrier for zero angular momentum; $E_r^{\rm gs}$ and $E_r^{\rm s}$ are the energy of the rotating ground state relative to the non-rotating macroscopic sphere and the rotational energy of the system at the saddle point, respectively. The angular momentum dependence of Γ_Z is taken into account by the addition of the rotational energy $E_r^{\rm s} = \hbar^2\ell(\ell+1)/2\Im_{saddle}$ to the conditional barrier B_Z for zero angular momentum, where $\Im_{saddle}$ is the moment of inertia about the axis perpendicular to the symmetry axis of the nucleus at the conditional saddle. The rotational energy of the saddle point $E_r^{\rm s}$ was calculated by assuming a configuration

of two nearly-touching spheres separated by 2 fm. The energy of the rotating ground state $E_r^{\rm gs}$ was calculated with the RFRM by Sierk [29]. The integral over the level density at the conditional saddle was carried out by means of a canonical expansion which also defines the saddle-point temperature T_Z as $1/T_Z = \partial[\ln \rho^*(x)]/\partial x \mid_{x=E-B_Z-E_r^s}$.

The neutron decay width Γ_n and proton decay width Γ_p can be written as

$$\Gamma_n = \frac{2mR^2g'}{\hbar^2 2\pi\rho(E-E_r^{\rm gs})}\int_0^{E-B_n-E_r^{\rm gs}} \varepsilon\,\rho(E-B_n-E_r^{\rm gs}-\varepsilon)\,d\varepsilon$$
$$\approx KT_n^2\,\frac{\rho(E-B_n-E_r^{\rm gs})}{\rho(E-E_r^{\rm gs})}, \qquad (5)$$

and

$$\Gamma_p = \frac{2mR^2g'}{\hbar^2 2\pi\rho(E-E_r^{\rm gs})}\int_{\varepsilon_C}^{E-B_p-E_r^{\rm gs}} \varepsilon(1-\frac{\varepsilon_C}{\varepsilon})\,\rho(E-B_p-E_r^{\rm gs}-\varepsilon)\,d\varepsilon$$
$$\approx KT_p^2\,\frac{\rho(E-B_p-\varepsilon_C-E_r^{\rm gs})}{\rho(E-E_r^{\rm gs})}, \qquad (6)$$

respectively. In the expressions above, $\rho(E-B_n-E_r^{\rm gs}-\varepsilon)$ is the level density of the residual nucleus after neutron emission; $\rho(E-B_p-E_r^{\rm gs}-\varepsilon)$ is the level density of the residual nucleus after proton emission; B_n is the neutron separation energy and B_p the proton separation energy; ε_C is the Coulomb barrier which an outgoing proton has to overcome (calculated in this work with the empirical formula given in [30]), ε is the kinetic energy of the emitted particle (neutron or proton); m is its mass; g' is its intrinsic spin degeneracy (g'=2); R is the radius of the nucleus from which it has been emitted; $K = 2mR^2g'/\hbar^2$; and T_n and T_p are the temperatures of the residual nuclei after neutron and proton emission, defined at the residual excitation energies $(E-B_n-E_r^{\rm gs})$ and $(E-B_p-\varepsilon_C-E_r^{\rm gs})$, respectively.

The formalism presented above requires the use of a specific level-density expression for the decay widths Γ_Z, Γ_n and Γ_p. As in previous work [7], for the level density at the saddle point we have used the approximate Fermi gas expression $\rho^*(E) \propto \exp\left(2\sqrt{a_Z E}\right)$, where E is the internal excitation energy of the system, and a_Z is the level density parameter at the conditional saddle-point. For the level density contained in the decay widths Γ_n and Γ_p, the standard Fermi gas expression is not adequate, however, since for ^{70,76}Se nuclei and their

immediate neighbors, the shell effects at their ground states are substantial (as large as -3 to -5 MeV) [31]. For the excitation energy range explored in this work, the shell effects can be, and are, taken into account by using the asymptotic form [32, 33]:

$$\rho(E) \propto \exp\left(2\sqrt{a_n(E-\Delta_{\rm shell})}\right), \tag{7}$$

where E represents the internal excitation energy, and $\Delta_{\rm shell}$ is the shell effect, of the nucleus concerned (the compound nucleus, or the residual nucleus after neutron or proton emission); a_n is the level density parameter of the nucleus at its ground state shape, which is taken to be $a_n = A/8$ (MeV^{-1}) in our analysis.

Individual excitation functions were analyzed by means of a two-parameter fit for each fragment. The two free parameters are the conditional barrier B_Z and the ratio of the level density parameter at the saddle point to that of the ground state (a_Z/a_n). In order to account for the excitation energy spread of the compound nucleus resulting from the projectile energy lost in the C target (1.0 mg/cm^2), the average cross section for a flat energy distribution over a small energy range $[E_0 - \delta E, E_0 + \delta E]$ as calculated using the recipe of [7], is substituted for σ_Z in Eq. (1) in our fitting routine to calculate the fission cross section. The fits are good at all Z-values and for the entire excitation energy range, as shown in Figs. 7 and 8 by the solid lines. The quality of the fits can also be seen in Figs. 5 and 6 where charge distributions obtained from the experiment (symbols) are compared with those obtained from the fits (solid lines).

B Global fitting and extracted parameters

The extracted barriers B_Z and the ratio of the level density parameters (a_Z/a_n), obtained from the individual fits (i.e., the two-parameter fits of individual excitation functions in the previous section) are shown in Fig. 10, and listed in Table IV for the compound nuclei ^{70,76}Se. The barriers increase as the exit channel becomes more symmetric and peak at symmetry (Z=17). This is the trend expected for the compound nuclei ^{70,76}Se which lie below the Businaro-Gallone point [5].

The values of a_Z/a_n extracted from the individual fits for ^{70}Se are in the range of 0.95 to 0.99 and most values are centered around ~0.96. The ratio a_Z/a_n decreases somewhat as a function of mass asymmetry. But the values of a_Z/a_n extracted for ^{76}Se increase as a function of mass asymmetry and span the range of 0.97 to 1.03. Values of the extracted barriers B_Z for ^{70}Se are lower than those for ^{76}Se. Furthermore, the odd-even staggering in the fragment yields (see Figs. 5 and 6) is manifested in both fit parameters, a_Z/a_n and B_Z.

It is not clear why there should be a (fluctuating) Z dependence to a_Z/a_n. Therefore, in order to remove these fluctuations from a_Z/a_n, we have attempted a simultaneous fit of all excitation functions for a given compound nucleus. In this "global fit", the level density parameter a_Z/a_n is assumed to be the same for all Z values. The simultaneous fitting effectively decreases the number of the free parameters from 30 for the individual fits to 16 for the global fits. For ^{76}Se, we fit the 15 experimental excitation functions with Eq. (1) using the 16 free parameters B_Z(Z = 5, 6, ...19), and a_Z/a_n. The other fixed parameters, such as the level density parameter a_n and the maximum angular momentum ℓ_{max}, were kept the same values as those utilized in the individual fits (section IV A). The fits for all asymmetries are good over the entire excitation energy range, as shown by the solid lines in the right panel of Fig. 11.

For ^{70}Se, the fits are also good, except for the two excitation functions of boron and carbon (shown as the dashed lines in the left panel of Fig. 11). The calculated excitation functions of boron and carbon do not describe the experimental data for the three higher excitation energies. This may be due to the larger background contaminations present in these light elements. In particular, the strong anisotropic component from deep-inelastic scattering makes it difficult to extract reliably the weaker isotropic component for Z-values equal to or smaller than that of the target. In addition, larger backgrounds were observed in the energy spectra for these two elements. Thus excitation functions for boron and carbon were ignored for the global fitting for ^{70}Se.

The extracted parameters from the global fits for ^{70,76}Se are shown in Fig. 10 and also listed in Table V. The extracted ratios of the level density parameter (a_Z/a_n) are 0.96 and

1.00 for ^{70}Se and ^{76}Se, respectively, which are close to the average values of the extracted a_Z/a_n from the individual fits. But there still exists the difference, 0.04, between the values of the ratio a_Z/a_n for ^{70}Se and ^{76}Se. The reason for this difference is not clear.

The barriers extracted from these two fit methods are very close for ^{70}Se but now the odd-even behavior is contained completely and consistently in B_Z. For ^{76}Se the barriers from the global fits change more smoothly than the barriers extracted from the individual fits with increasing the asymmetries. In summary, both fit methods give consistent asymmetric fission barriers but barriers from the global fits reflect the behavior of the fragments yields more closely.

The extracted values for the conditional barriers contain several uncertainties. In our fits, $a_n = A/8$ (MeV^{-1}) was chosen. When the level density parameter a_n decreases from $A/8$ to $A/9$, the values of the extracted barriers increase by 1.5% (^{70}Se) and 2.4% (^{76}Se) on average. The errors in the extracted barriers resulting from the uncertainty in the projectile energy loss in the target are not larger than 1%. The uncertainties from the absolute cross sections carried over through the fitting procedures are less than 1% on average. Thus, we assign a possible overall uncertainty of $\pm 3\%$ for the barriers of ^{70,76}Se.

C Comparison with macroscopic nuclear models

The experimental macroscopic conditional barriers $B_Z^{\rm macro}$, i.e., the extracted barriers corrected for the shell effects, are

$$B_Z^{\rm macro} = B_Z - \Delta^n_{\rm shell}\,, \tag{8}$$

where $\Delta^n_{\rm shell}$ is the shell effect of the compound nucleus. The values of the shell effects were taken in this work to be the values given by Möller *et al.* [31]. Fig. 12 compares the experimental macroscopic barriers, as obtained by Eq. (8), with those calculated with the Rotating Liquid Drop Model (RLDM) and the Rotating Finite-Range Model (RFRM). The experimental data fall in between the the RFRM and the RLDM calculations, as for

the reactions ^{78,82,86}Kr + ^{12}C [7] and ^{86}Kr + ^{63}Cu [11]. For the compound nuclei ^{70}Se and ^{76}Se, the experimental macroscopic barriers are on average ~13% greater than the RFRM calculations; they are ~21% smaller than those from the RLDM.

In a recently developed Thomas-Fermi Model (TFM) [34, 35], Myers and Swiatecki identified an extra binding energy term, the so-called congruence energy, which is related to $I = (N - Z)/A$ and nuclear shapes. For intermediate mass nuclei, the saddle shape is highly necked-in, and the congruence energy at the saddle point nearly doubles. The fission barriers correspondingly decrease by several MeV, as compared to the case in which the congruence energy of the saddle is assumed to be the same as that of the ground state. To determine if our data provide evidence for the near-doubling of the congruence energy for very necked-in saddle-point shapes, a comparison of the experimental symmetric fission barriers to Thomas-Fermi model calculations is shown in Fig. 13 and Table VI for ^{70,76}Se and ^{90,94,98}Mo [7]. The measured symmetric fission barriers for all the five systems lie somewhat below but closer to Thomas-Fermi barriers which include the shape-dependent congruence energy. This comparison seems to support qualitatively Myers and Swiatecki's argument for the congruence energy, but a quantitative discrepancy remains.

In the above comparison we have left out the barrier data for ^{75}Br from ref. [6]. We now have some concerns regarding accuracy of the low energy part of the excitation functions reported in [6] for ^{75}Br. The target used in the experiment was not as pure as the one used in the later Mo and Se experiments [16], and the contaminations from other potential sources might not have been dealt with adequately. Thus the reported cross sections at the lowest energies may be substantially higher than the actual values. This may result in extracted barriers lower than the actual values by as much as 2 MeV.

V. SCALING LAW IN THE COMPLEX FRAGMENT EMISSION PROBABILITY

In this section, we will use the transition state theory to scale the experimental fission excitation functions to search for possible deviations from the transition state rates. According to a procedure introduced in refs. [7, 12, 14], the experimental complex fragment emission probability can be replotted using the following equation:

$$\ln\left[\frac{\sigma_Z}{\sigma_0}\Gamma_T\frac{2\pi\rho(E-E_r^{gs})}{T_Z}\right]\Big/2\sqrt{a_n}=\frac{\ln R_f}{2\sqrt{a_n}}=\sqrt{\frac{a_Z}{a_n}(E-B_Z-E_r^s)}\,, \qquad (9)$$

where T_Z is the temperature at the conditional saddle, $\rho(E-E_r^{gs})$ is the level density of the compound nucleus, E_r^{gs} and E_r^s are the energy of the rotating ground state relative to the non-rotating macroscopic sphere and the rotational energy of the system at the saddle point, respectively. a_Z and a_n are the saddle and ground state level density parameters, and B_Z is the conditional barrier for zero angular momentum. Thus, plotting the left hand side of this equation versus the square root of the intrinsic excitation energy $\sqrt{E-B_Z-E_r^s}$ over the saddle should result in a straight line, and the slope should give the square root of a_Z/a_n. Notice that the shell effects of the Se nuclei and their daughters after neutron or proton emission are properly accounted for by using the level density expression given by Eq. (7). The above hypothesis can be tested by fitting the excitation functions for an extensive range of complex fragment atomic numbers for the compound nuclei ^{70,76}Se measured in the present work, and by scaling the measured excitation functions with Eq. (9). In the following scaling, E_r^{gs} and E_r^s in Eq. (9) were taken to be the average values. Using the same maximum angular momentum ℓ_{max} as used in the best fit to the excitation functions, one can calculate $<\ell^2> = \ell_{max}^2/2$ and then the averages of E_r^{gs} and E_r^s according to the same procedure as in the barrier extraction. In Fig. 14, all the excitation functions associated with each of the two compound nuclei are plotted according to Eq. (9). We see all the excitation functions for each Z value fall on a straight line which has a slope near unity and passes closely through zero. In Fig. 15(a), we plot the logarithm of the reduced

mass-asymmetric fission rate $\ln R_f$ versus the square root of the internal excitation energy for fragment $Z = 12$ emitted from the two compound nucleus isotopes. We can see that the excitation functions are straight lines, but with different slopes for the two different mass compound nuclei. After the A dependence is removed by dividing by a factor of $2\sqrt{a_n}$, as suggested in Eq. (9), the two lines collapse onto a single straight line [see Fig. 15(b)]. Similar results are obtained for all the other Z-values. Fig. 15 shows the sensitivity of the excitation functions to the mass number A of compound nucleus. All 31 excitation functions for fragments with $Z = 5$ to 20 for the two compound nuclei collapse onto a single straight line, as shown in Fig. 16. The collapse of all the experimental excitation functions for the two systems onto a single straight line is in excellent agreement with the transition state formalism.

VI. SUMMARY AND CONCLUSIONS

Excitation functions for complex fragments with $4<Z<21$ have been measured over the range of bombarding energy from E/A = 6-14 MeV for the ^{58,64}Ni + ^{12}C reactions. Velocity and angular distributions were utilized to isolate the complex fragments arising from the binary decay of a compound nucleus. Mass asymmetric fission barriers for the compound nuclei ^{70,76}Se have been obtained by fitting the excitation functions with a transition state formalism. Values of the measured barriers lie between the calculations of the RFRM and the RLDM. The measured symmetric fission barriers are slightly lower, but consistent with the Thomas-Fermi fission barriers calculated with inclusion of the shape-dependent congruence energy. The experimental excitation functions for the two compound nuclei are shown to scale according to transition state predictions.

The authors wish to thank A. J. Sierk and W. J. Swiatecki for supplying the RFRM and the Thomas-Fermi Model calculations. This work was supported by the Director, Office of Energy Research, Office of High Energy and Nuclear Physics, Nuclear Physics Division of the U.S. Department of Energy, under Contract No. DE-AC03-76SF00098.

REFERENCES

[1] Permanent address: Institute for Heavy Ion Physics, Department of Technical Physics, Peking University, Beijing 100871, China.

[2] Current Address: Look Ease Enterprises Ltd., Dominion Centre, 43-45, Queen's Road East, Hong Kong.

[3] Current Address: Syagen Technology, 1411 Warren Ave., Tustin, CA 92780, USA.

[1] L.G. Moretto and G.J. Wozniak, Annual Reviews of Nuclear and Particle Science, J.D. Jackson, Ed., Annual Reviews, Inc., Palo Alto, CA, May 1993, and references therein.

[2] L.G. Moretto and G.J. Wozniak, Prog. part. Nucl. Phys. **21** (1988) 401, and references therein.

[3] L.G. Moretto, Phys. Lett. **B40** (1972) 185.

[4] L.G. Moretto, Nucl. Phys. **A247** (1975) 211.

[5] U.L. Businaro and S. Gallone, Nuovo Cimento **1** (1955) 629; **1** (1955) 1277.

[6] D.N. Delis, Y. Blumenfeld, D.R. Bowman, N. Colonna, K. Hanold, K. Jing, M. Justice, J.C. Meng, G.F. Peaslee, G.J. Wozniak and L.G. Moretto, Nucl. Phys. **A534** (1991) 403.

[7] K.X. Jing, L.G. Moretto, A.C. Veeck, N. Colonna, I. Lhenry, K. Tso, K. Hanold, W. Skulski, Q. Sui and G.J. Wozniak, Nucl. Phys. **A645** (1999) 203.

[8] M.A. McMahan, L.G. Moretto, M.L. Padgett, G.J. Wozniak, L.G. Sobotka and M.G. Mustafa, Phys. Rev. Lett. **54** (1985) 1995.

[9] A.J. Sierk, Phys. Rev. Lett. **55** (1985) 582.

[10] A.J. Sierk, Phys. Rev. **C33** (1986) 2039.

[11] J. Boger and J. M. Alexander, Phys. Rev. **C50** (1994) 1006.

[12] L.G. Moretto, K.X. Jing, R. Gatti and G.J. Wozniak, Phys. Rev. Lett. **75** (1995) 4186.

[13] Th. Rubehn, K.X. Jing, L.G. Moretto, L. Phair, K. Tso and G.J. Wozniak, Phys. Rev. **C54** (1996) 3062.

[14] L.G. Moretto, K.X. Jing and G.J. Wozniak, Phys. Rev. Lett. **74** (1995) 3557.

[15] Z.Q. Xie, C.M. Lyneis, R.S. Lam and S.A. Lundgren, Rev. Sci. Instrum. **62** (1991) 775.

[16] A.C. Veeck, K.X. Jing, Q. Sui, L.G. Moretto, and G.J. Wozniak, Nucl. Instr. Meth. **B108** (1996) 159.

[17] M.A. McMahan, G.J. Wozniak, C.M. Lyneis, D.R. Bowman, R.J. Charity, Z.H. Liu, L.G. Moretto, W.L. Kehoe, A.C. Mignerey and M.N. Namboodiri, Nucl. Instr. Meth. **A253** (1986) 1.

[18] W.L. Kehoe, A.C. Mignerey, A. Moroni, I. Iori, G.F.Peaslee, N. Colonna, K. Hanold, D.R. Bowman, L.G. Moretto, M.A. McMahan, J.T. Walton and G.J. Wozniak, Nucl. Instr. Meth. **A311** (1992) 258.

[19] M.A. McMahan, R.F. Lebed and B. Feinberg, The 1989 IEEE Particle Accelerator Conference, Chicago, Ill., March 1989.

[20] R.J. Charity, D.R. Bowman, Z.H. Liu, R.J. McDonald, M.A. McMahan, G.J. Wozniak, L.G. Moretto, S. Bradley, W.L. Kehoe and A.C. Mignerey, Nucl. Phys. **A476** (1988) 516.

[21] V.E. Viola, K. Kwiatkowski and M. Walker, Phys. Rev. **C31** (1985) 1550.

[22] R.J. Charity, M.A. McMahan, G.J. Wozniak, R.J. McDonald, L.G. Moretto, D.G. Sarantites, L.G. Sobotka, G. Guarino, A. Pantaleo, L. Fiore, A. Gobbi and K.D. Hildenbrand, Nucl. Phys. **A483** (1988) 371.

[23] N. Bohr and J.A. Wheeler, Phys. Rev. **56** (1939) 426.

[24] L.G. Moretto, Physics and Chemistry of Fission 1973, (Vienna: International Atomic Energy Agency, 1974) I, p. 329.

[25] V.F. Weisskopf and P.H. Ewing, Phys. Rev. **57** (1940) 472.

[26] R.J. Charity, J.R. Leigh, J.J.M. Bokhorst, A. Chatterjee, G.S. Foote, D.J. Hinde, J.O. Newton, S. Ogaza and D. Ward, Nucl. Phys. **A457** (1986) 441.

[27] J. van der Plicht, H.C. Britt, M.M. Fowler, Z. Fraenkel, A. Gavron, J.B. Wilhelmy, F. Plasil, T.C. Awes and G.R. Young, Phys. Rev. **C28** (1983) 2022.

[28] R. Bass, Phys. Rev. Lett. **39** (1977) 265; Nucl. Phys. **A231** (1974) 45.

[29] A.J. Sierk, private communication, July, 1998.

[30] W.E. Parker, M. Kaplan, D.J. Moses, G. La Rana, D. Logan, R. Lacey, J.M. Alexander, D.M. de Castro Rizzo, P. DeYoung, R.J. Welberry and J.T. Boger, Phys. Rev. **C44** (1991) 774.

[31] P. Möller, J.R. Nix, W.D. Myers and W.J. Swiatecki, Los Alamos National Laboratory, LA-UR-3083 (1994).

[32] N. Rosenzweig, Phys. Rev. **108** (1957) 817.

[33] J.R. Huizenga and L.G. Moretto, Ann. Rev. Nucl. Sci. **22** (1972) 427.

[34] W. D. Myers and W. J. Swiatecki, Nucl. Phys. **A601** (1996) 141.

[35] W. D. Myers and W. J. Swiatecki, Nucl. Phys. **A612** (1997) 249.

[36] W. J. Swiatecki, private communication, March, 1998.

E_{beam} (AMeV)	14.29	12.91	11.59	10.35	9.17	8.07	7.03	6.07
E (MeV)	141.6± 1.7	127.7± 1.9	114.5± 2.0	102.0± 2.1	90.2± 2.3	79.0 ± 2.4	68.5± 2.6	58.8 ± 2.8
Z	σ_Z (mb)							
5	11.73±3.17	9.61±2.59	7.45±2.01	5.20±1.40	2.24±0.60	1.18±0.32	0.32±0.11	$(5.6\pm2.0)10^{-2}$
6	29.90±8.07	24.36±6.58	19.43±5.25	16.52±4.46	9.15±2.47	5.41±1.46	2.07±0.73	0.40±0.14
7	10.05±2.81	8.35±2.26	6.98±1.89	4.89±1.32	2.16±0.58	1.15±0.31	0.28±0.10	$(5.1\pm1.8)10^{-2}$
8	10.95±3.06	9.02±2.44	7.69±2.15	5.85±1.58	2.80±0.76	1.54±0.41	0.39±0.14	$(8.1\pm2.8)10^{-2}$
9	4.07±1.14	3.29±0.89	2.65±0.74	2.00±0.54	0.69±0.19	0.33±0.09	$(6.9\pm2.4)10^{-2}$	$(6.4\pm2.3)10^{-3}$
10	6.96±1.88	5.45±1.20	4.02±0.92	2.70±0.73	1.10±0.30	0.44±0.12	$(8.8\pm3.1)10^{-2}$	$(8.3\pm3.0)10^{-3}$
11	5.14±1.18	3.86±0.85	2.83±0.65	2.10±0.46	0.92±0.25	0.29±0.07	$(5.3\pm1.8)10^{-2}$	$(4.5\pm1.7)10^{-3}$
12	6.45±1.48	4.93±1.08	3.79±0.87	2.82±0.62	1.20±0.32	0.42±0.10	$(7.1\pm2.4)10^{-2}$	$(6.0\pm2.2)10^{-3}$
13	4.66±1.07	3.60±0.79	2.81±0.65	1.83±0.40	0.84±0.24	0.27±0.07	$(4.4\pm1.6)10^{-2}$	$(3.5\pm1.5)10^{-3}$
14	6.71±1.54	4.87±1.07	3.57±0.82	2.55±0.59	1.30±0.35	0.38±0.10	$(5.5\pm2.0)10^{-2}$	$(5.5\pm2.3)10^{-3}$
15	4.26±0.98	3.12±0.69	2.31±0.53	1.61±0.37	0.89±0.29	0.21±0.07	$(3.2\pm1.1)10^{-2}$	$(2.4\pm1.1)10^{-3}$
16	5.13±1.18	3.63±0.83	2.85±0.80	2.06±0.58	1.19±0.42	0.28±0.10	$(3.8\pm1.5)10^{-2}$	$(2.6\pm1.4)10^{-3}$
17	4.02±0.92	3.02±0.70	2.22±0.62	1.67±0.48	0.90±0.34	0.20±0.08	$(3.3\pm1.6)10^{-2}$	$(2.3\pm1.3)10^{-3}$
18	4.30±0.99	3.32±0.76	2.55±0.71	1.79±0.52	0.74±0.28	0.24±0.09	$(3.8\pm1.8)10^{-2}$	$(2.2\pm1.2)10^{-3}$
19	4.62±1.06	3.37±0.78	2.58±0.72	1.66±0.48	0.56±0.21	0.21±0.08	$(3.9\pm2.0)10^{-2}$	
20	6.17±1.42	4.05±0.93	3.02±0.85	2.12±0.61	0.69±0.26	0.22±0.08		

TABLE I: The experimental cross sections of the isotropic component in the angular distributions as a function of the fragment Z-value and the excitation energy E of the compound nucleus ^{70}Se produced in the ^{58}Ni + ^{12}C reaction at eight bombarding energies (E_{beam}). The excitation energy E is given as the centroid energy at the center of the C target (1.0 mg/cm^2), and the errors given in E are the energy loss in half the thickness of the target. The errors shown for the cross sections include both the statistical and systematic ones.

E_{beam} (AMeV)	12.95	10.62	9.53	8.51	7.54	6.63
E (MeV)	137.2± 1.7	113.4± 1.9	102.4± 2.0	91.9± 2.2	82.0± 2.3	72.6± 2.5
Z	σ_Z (mb)					
5	8.92±2.50	4.96±1.34	2.91±0.79	1.78±0.48	0.69±0.21	0.24±0.08
6	17.84±4.99	8.23±2.22	5.95±1.61	3.43±0.93	1.65±0.49	0.60±0.21
7	5.44±1.58	2.98±0.80	1.77±0.48	0.90±0.24	0.29±0.09	0.13±0.05
8	6.13±1.78	2.58±0.70	1.50±0.41	0.72±0.19	0.26±0.08	$(4.6\pm1.6)10^{-2}$
9	2.68±0.83	1.25±0.35	0.66±0.18	0.24±0.65	$(8.0\pm2.5)10^{-2}$	$(1.1\pm0.4)10^{-2}$
10	3.61±0.97	1.15±0.33	0.68±0.18	0.30±0.08	$(8.2\pm2.5)10^{-2}$	$(1.2\pm0.4)10^{-2}$
11	3.14±0.85	0.96±0.28	0.54±0.15	0.19±0.06	$(5.2\pm1.4)10^{-2}$	$(8.3\pm2.7)10^{-3}$
12	3.55±0.96	0.98±0.28	0.52±0.15	0.16±0.05	$(4.2\pm1.0)10^{-2}$	$(6.5\pm2.2)10^{-3}$
13	2.38±0.67	0.77±0.22	0.38±0.11	0.12±0.04	$(2.6\pm0.7)10^{-2}$	$(3.7\pm1.4)10^{-3}$
14	2.78±0.78	0.76±0.22	0.37±0.12	0.11±0.04	$(2.3\pm0.7)10^{-2}$	$(3.7\pm1.4)10^{-3}$
15	2.06±0.70	0.62±0.18	0.28±0.09	$(9.1\pm2.9)10^{-2}$	$(1.8\pm0.7)10^{-2}$	$(2.2\pm1.1)10^{-3}$
16	2.66±0.91	0.63±0.21	0.27±0.09	$(8.2\pm2.8)10^{-2}$	$(1.5\pm0.6)10^{-2}$	$(2.3\pm1.3)10^{-3}$
17	2.66±0.90	0.64±0.22	0.27±0.10	$(8.5\pm2.9)10^{-2}$	$(1.4\pm0.5)10^{-2}$	$(2.0\pm1.1)10^{-3}$
18	2.57±0.87	0.66±0.23	0.30±0.12	$(9.5\pm3.7)10^{-2}$	$(1.5\pm0.6)10^{-2}$	$(2.3\pm1.3)10^{-3}$
19	2.19±0.74	0.62±0.21	0.30±0.11	0.10±0.04	$(1.8\pm0.8)10^{-2}$	$(2.2\pm1.2)10^{-3}$

TABLE II: Same as in Table I for the compound nucleus ^{76}Se produced in the ^{64}Ni + ^{12}C reaction at six bombarding energies.

	$^{58}Ni + ^{12}C \longrightarrow ^{70}Se$		$^{64}Ni + ^{12}C \longrightarrow ^{76}Se$		
E_{beam}	$\ell_{max}(\hbar)$	$\ell_{max}(\hbar)$	E_{beam}	$\ell_{max}(\hbar)$	$\ell_{max}(\hbar)$
(AMeV)	(Bass)	(Fits)	(AMeV)	(Bass)	(Fits)
14.29	41.1	43			
12.91	41.1	42	12.95	43.7	45
11.59	41.1	41			
10.35	41.1	40	10.62	43.7	43
9.17	40.2	39	9.53	43.2	42
8.07	37.6	38	8.51	40.7	41
7.03	34.9	36	7.54	38.3	39
6.07	32.3	33	6.63	35.8	36

TABLE III: Values of the maximum angular momemtum for fusion associated with the $^{58}Ni + ^{12}C$ and $^{64}Ni + ^{12}C$ reactions. The column ℓ_{max}(Bass) shows the values predicted by the Bass Model [28]. The column ℓ_{max}(fits) shows the values used in the fits.

	$^{58}Ni + {}^{12}C \longrightarrow {}^{70}Se$			$^{64}Ni + {}^{12}C \longrightarrow {}^{76}Se$		
Z	B_Z(MeV)	a_Z/a_n	χ^2	B_Z(MeV)	a_Z/a_n	χ^2
5	26.21±0.30	0.988±0.008	0.97	26.87±0.55	0.988±0.012	0.12
6	25.28±0.30	0.985±0.008	3.90	27.02±0.59	0.984±0.013	1.32
7	28.56±0.29	0.966±0.008	2.44	30.28±0.55	0.969±0.013	1.41
8	28.97±0.29	0.957±0.008	3.84	32.32±0.55	0.985±0.013	0.19
9	31.98±0.28	0.946±0.007	1.69	35.15±0.51	0.984±0.012	0.87
10	32.50±0.28	0.963±0.007	0.74	35.74±0.52	0.986±0.012	0.24
11	33.46±0.26	0.955±0.006	0.67	37.09±0.49	0.991±0.012	0.29
12	33.45±0.25	0.958±0.006	0.65	38.28±0.48	1.006±0.011	0.61
13	34.33±0.27	0.952±0.006	0.37	39.25±0.47	1.002±0.011	0.53
14	34.17±0.28	0.959±0.006	0.77	39.87±0.52	1.010±0.012	0.64
15	35.09±0.29	0.952±0.010	1.22	40.44±0.58	1.007±0.013	0.28
16	34.97±0.32	0.956±0.007	1.90	41.25±0.63	1.025±0.015	0.48
17	35.16±0.34	0.950±0.007	1.27	41.58±0.58	1.031±0.014	0.48
18	35.11±0.34	0.954±0.007	0.88	41.16±0.63	1.024±0.014	0.60
19	35.20±0.43	0.959±0.006	0.63	40.45±0.62	1.009±0.014	0.22
20	35.15±0.50	0.973±0.009	0.92			

TABLE IV: Values of the mass-asymmetric fission barriers (B_Z) and the ratio of the level density parameters (a_Z/a_n) for the compound nuclei ^{70,76}Se, extracted from fitting the excitation functions with a transition state formalism. The uncertainties given are the standard errors solely arising from the uncertainties of the cross section. The uncertainties arising from the choice of these parameters are discussed in the text and not included in the table.

	$^{58}Ni + {}^{12}C \longrightarrow {}^{70}Se$		$^{64}Ni + {}^{12}C \longrightarrow {}^{76}Se$	
Z	B_Z(MeV)	a_Z/a_n	B_Z(MeV)	a_Z/a_n
5			27.19±0.32	0.996±0.006
6			27.41±0.33	0.996±0.006
7	28.48±0.17	0.963±0.003	31.40±0.35	0.996±0.006
8	29.17±0.22	0.963±0.003	32.78±0.32	0.996±0.006
9	32.57±0.18	0.963±0.003	35.64±0.32	0.996±0.006
10	32.50±0.16	0.963±0.003	36.14±0.32	0.996±0.006
11	33.74±0.16	0.963±0.003	37.30±0.31	0.996±0.006
12	33.63±0.18	0.963±0.003	37.96±0.30	0.996±0.006
13	34.75±0.19	0.963±0.003	39.06±0.30	0.996±0.006
14	34.34±0.21	0.963±0.003	39.37±0.32	0.996±0.006
15	35.55±0.19	0.963±0.003	40.07±0.33	0.996±0.006
16	35.25±0.26	0.963±0.003	40.27±0.34	0.996±0.006
17	35.75±0.28	0.963±0.003	40.45±0.33	0.996±0.006
18	35.49±0.27	0.963±0.003	40.20±0.36	0.996±0.006
19	35.38±0.24	0.963±0.003	39.98±0.37	0.996±0.006
20	34.73±0.28	0.963±0.003		

TABLE V: Values of the mass-asymmetric fission barriers (B_Z) and the ratio of the level density parameters (a_Z/a_n) for the compound nuclei ^{70,76}Se, extracted from global fitting. The uncertainties given are the errors arising from the uncertainties of the cross sections and also take into account both parameter correlations and non-linearities. The uncertainties arising from the choice of these parameters are discussed in the text and not included in the table.

Nuclei	Fissility	B^{TF}	Congruence	B^{TFC}	Shell	B_Z^{macro}	$B^{\mathrm{TFC}} - B_Z^{\mathrm{macro}}$
		(MeV)	(MeV)	(MeV)	(MeV)	(MeV)	(MeV)
^{70}Se	16.54	49.43	-7.64	41.79	-3.70	39.45	2.34
^{76}Se	15.59	53.98	-5.38	48.60	-4.08	44.53	4.07
^{90}Mo	19.79	50.93	-5.76	45.17	0.04	40.92	4.25
^{94}Mo	19.25	53.09	-4.88	48.21	0.12	44.68	3.53
^{98}Mo	18.85	55.15	-4.17	50.98	-2.98	45.84	5.14

TABLE VI: Values of the measured symmetric fission barriers (Z=17, see Table V) corrected for ground-state shell effects and the Thomas-Fermi model calculations that include the shape-dependent congruence energy. The second column is the fissility parameter which is defined as $Z^2/A(1 - 2.2I^2)$ where $I = (N - Z)/A$. B^{TF} is the Thomas-Fermi barrier calculated without inclusion of the shape dependence of the congruence energy. The fourth column (Congruence) is the amount by which the energy of the nucleus at the saddle point was decreased due to the shape dependence of the congruence energy. The B^{TFC} is the Thomas-Fermi barrier corrected for the congruence energy term. The next column (Shell) is the shell effect of the compound nucleus [31]. The seventh column is the experimental symmetric barrier (B_Z^{macro}) corrected for the shell effect to be compared with B^{TFC}. The eighth column shows the difference between the calculated and experimental barriers. All of the theoretically calculated results included in this table were provided by Swiatecki [36].

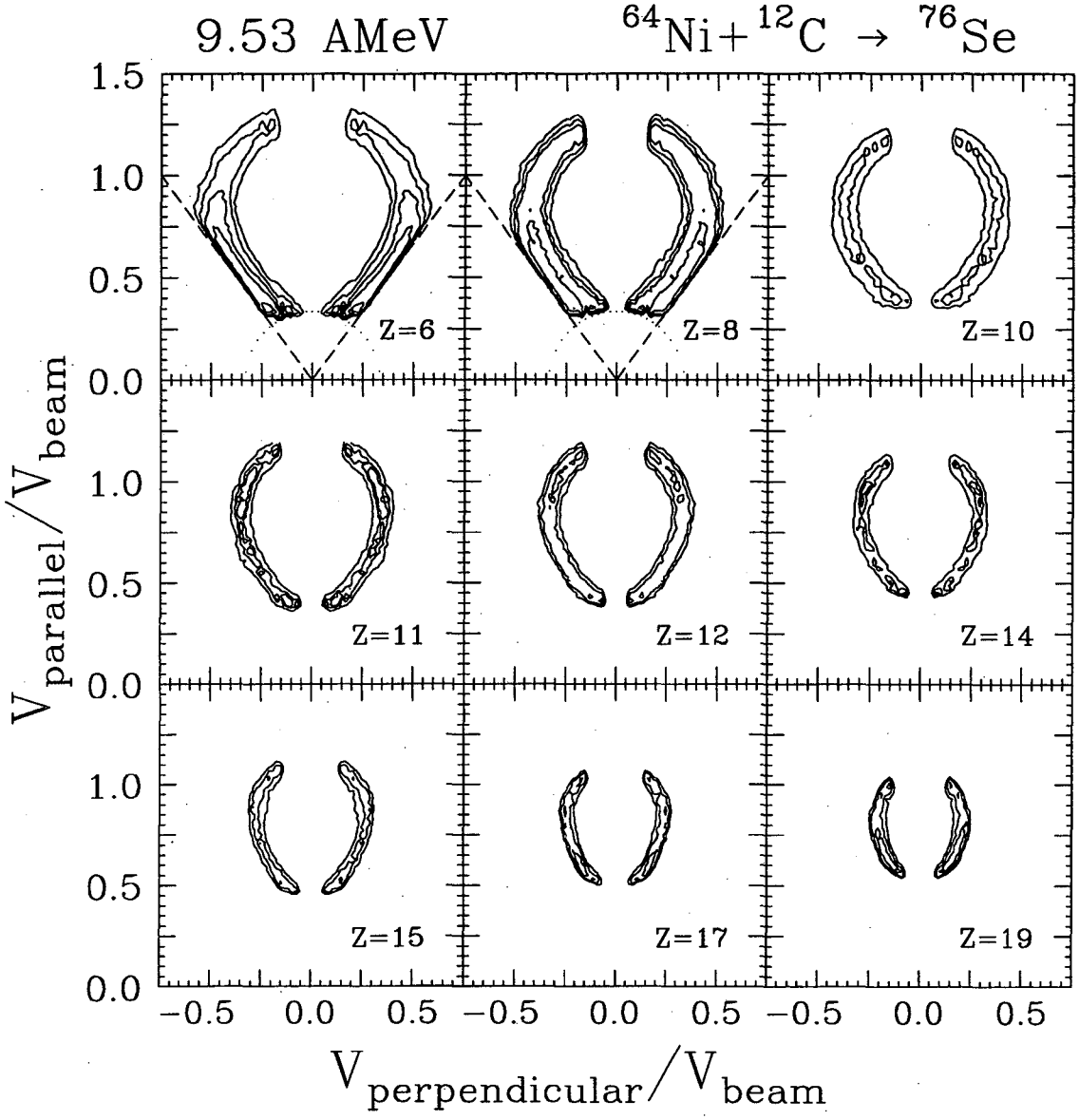

FIG. 1: Contours of the experimental cross section $\partial^2\sigma/\partial V_{\|}\partial V_{\perp}$ in the $V_{\|} - V_{\perp}$ plane for representative fragment Z-values detected in the reaction 9.53 AMeV ^{64}Ni + ^{12}C. The fragment velocities are expressed as a fraction of the beam velocity and the beam direction is vertical. The magnitudes of the contour levels indicated are relative. The dashed lines represent the limits of the geometrical coverage of the experimental device. The dotted lines show the energy thresholds of the detectors.

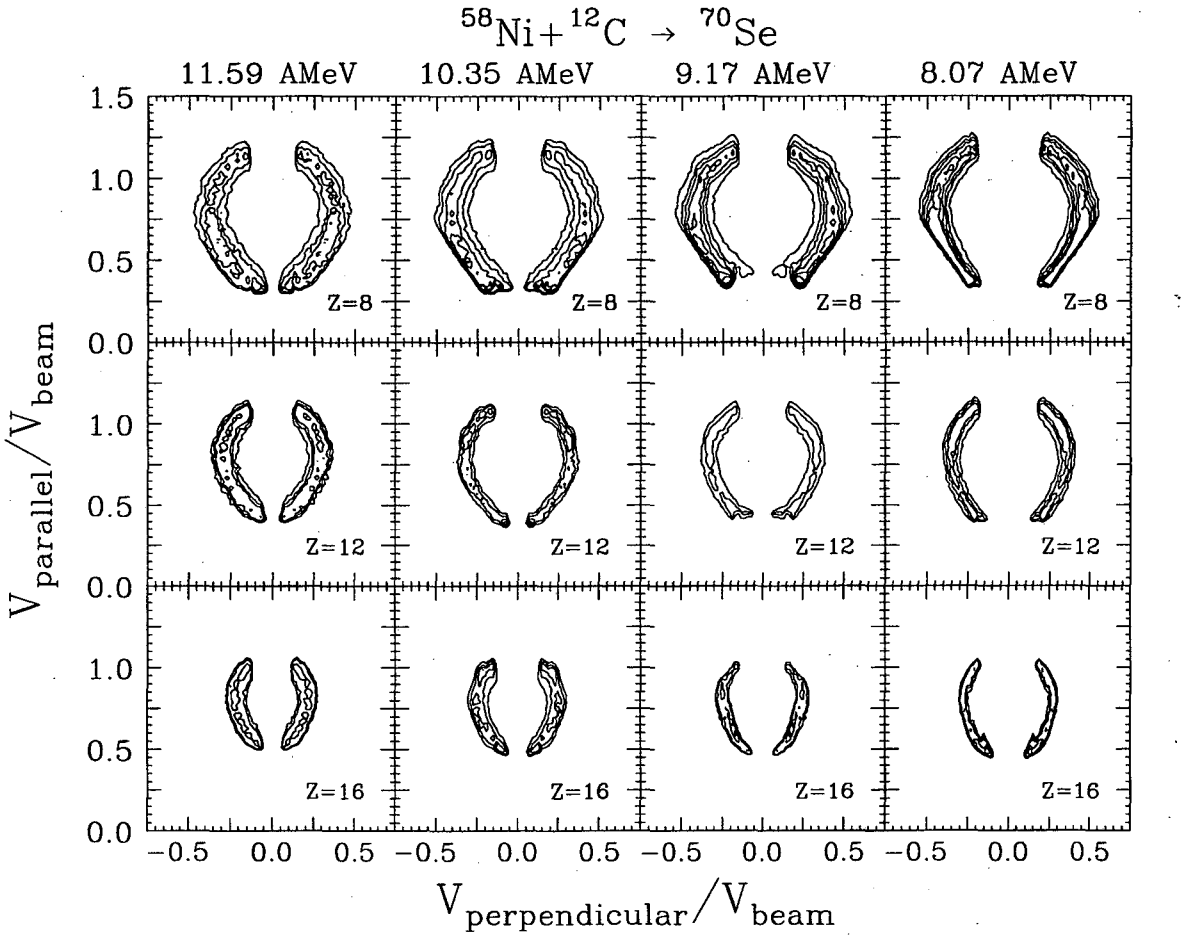

FIG. 2: Same as in Fig. 1, for the reactions ^{58}Ni + ^{12}C at four different bombarding energies.

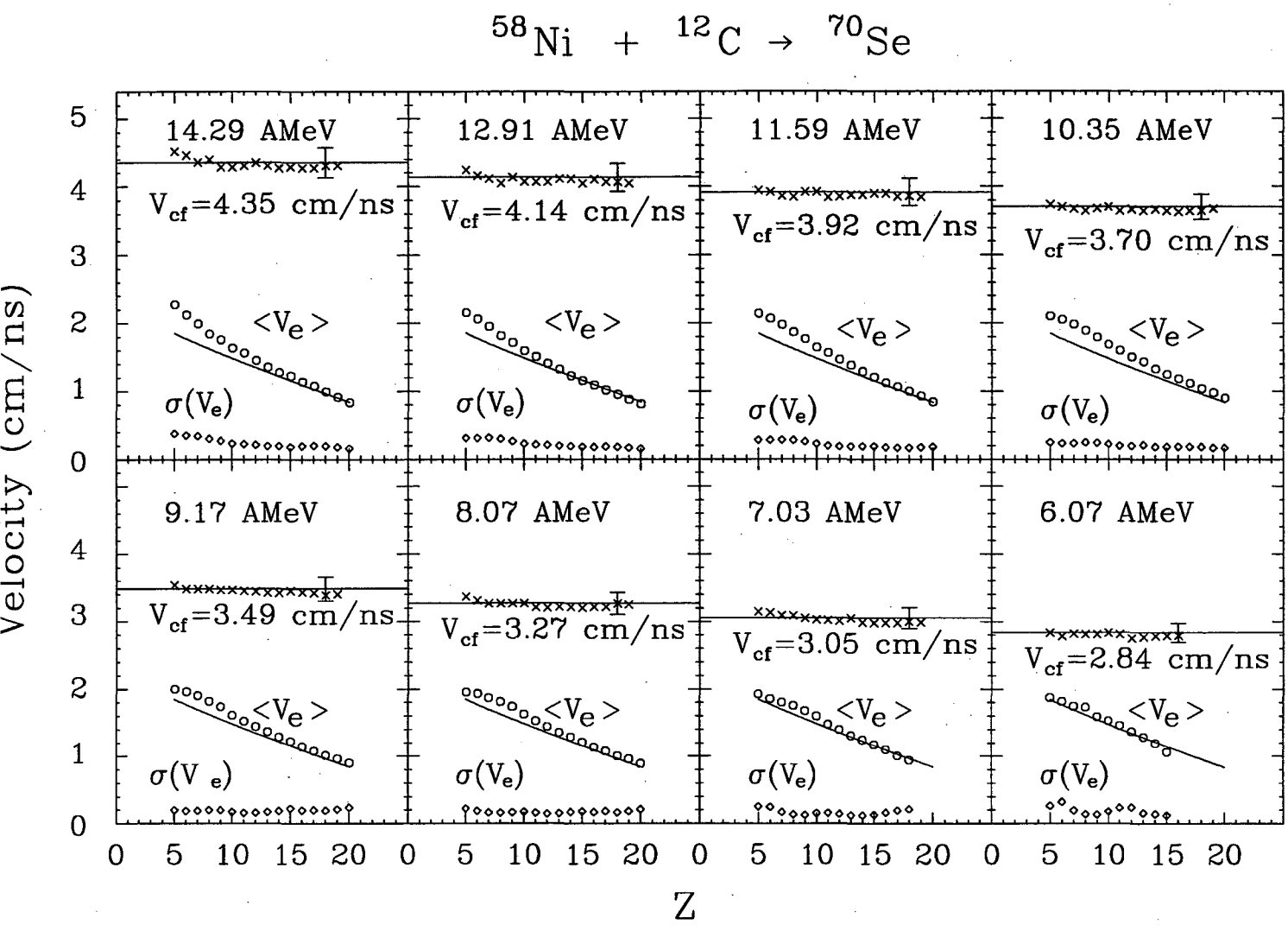

FIG. 3: Source velocities (×) were determined as the centers of the Coulomb rings (see Fig. 2) for each Z-species produced in the ^{58}Ni + ^{12}C reactions at bombarding energies E = 14.29, 12.91, 11.59, 10.35, 9.17, 8.07, 7.03 and 6.07 AMeV. The single large error bar for each bombarding energy indicates the possible systematic error. The complete fusion velocity V_{cf} is shown in the plot as the horizontal line. In the lower portions of each octant are shown the average experimental emission velocities $<V_e>$ (○) determined as the radii of the Coulomb rings. A simple calculation based on the Viola systematics [21] (solid line) are also shown for comparison. The second moments $\sigma(V_e)$ of the velocity distributions in the source frame are shown by the diamonds (◇).

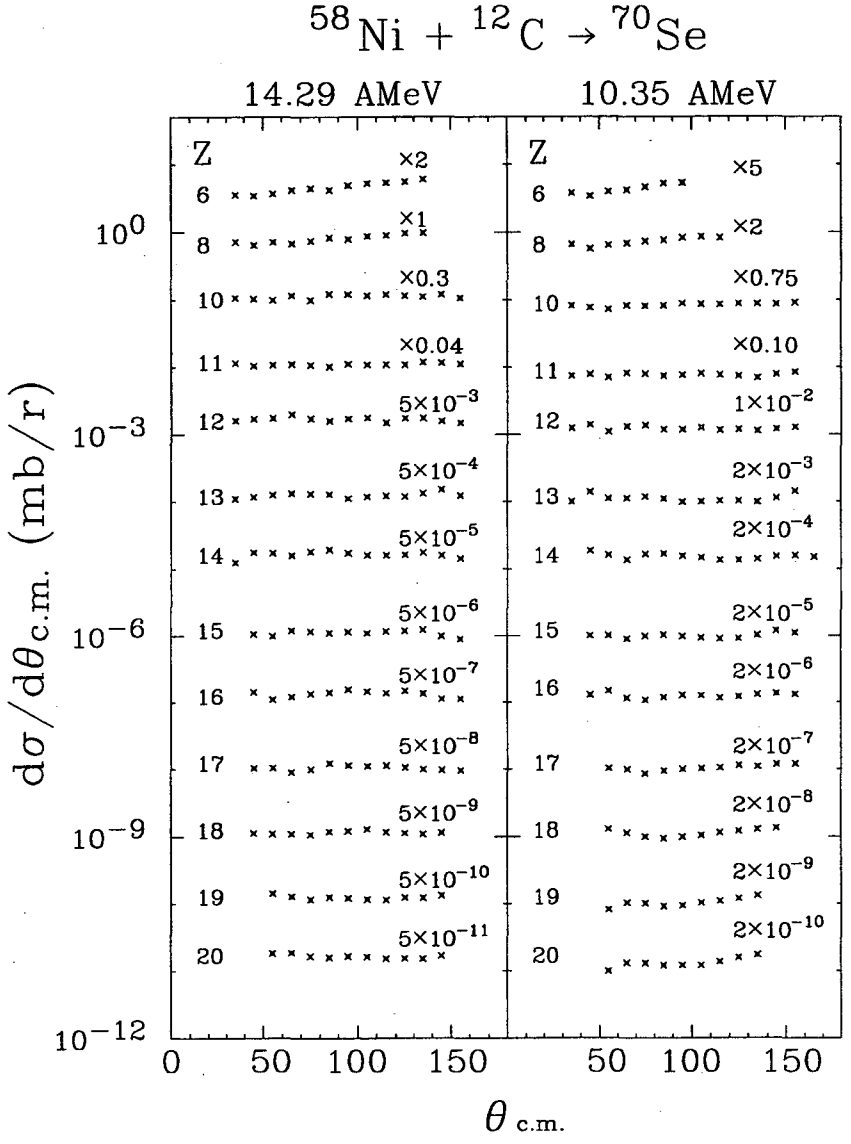

FIG. 4: Representative angular distributions $d\sigma/d\theta_{c.m.}$ in the frame of the source system for the ^{58}Ni + ^{12}C reactions at E = 14.29 and 10.35 AMeV. The numbers to the right are the factors by which the angular distributions are multiplied for visual clarity.

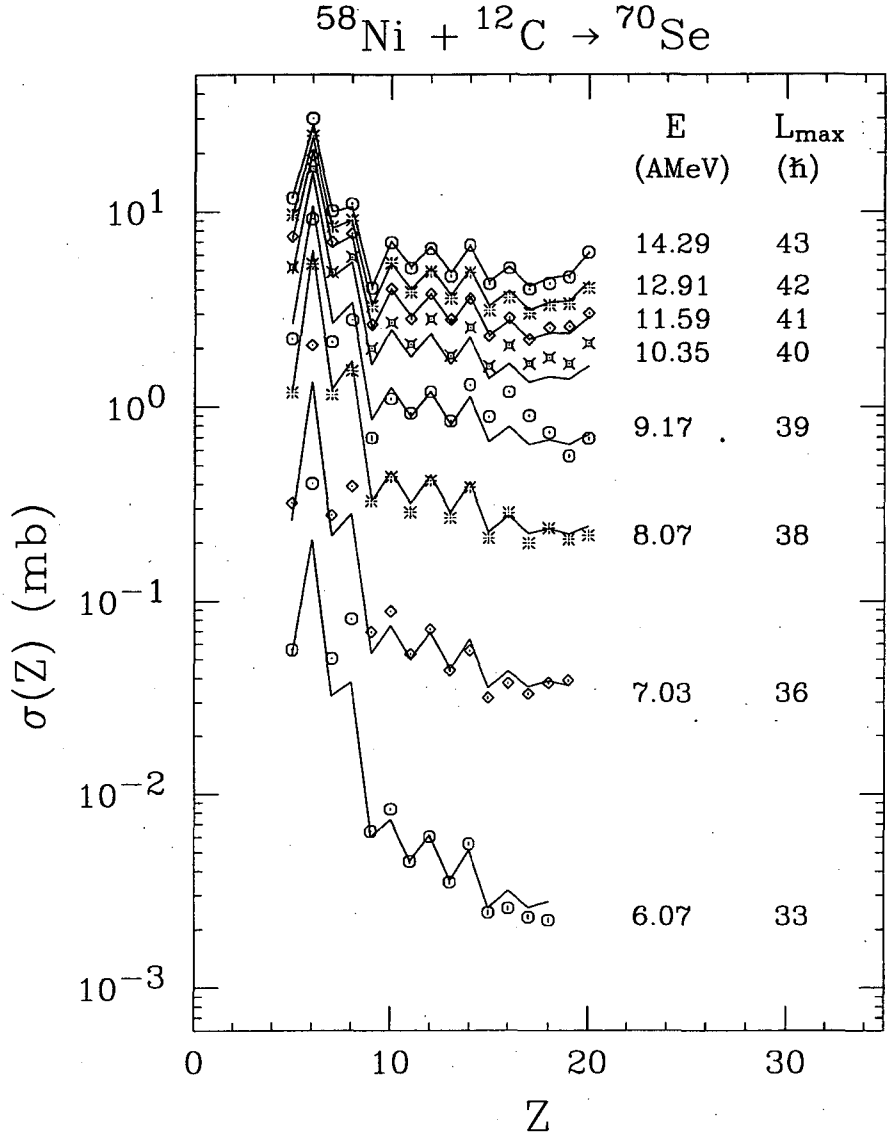

FIG. 5: Charge distributions of the isotropic component in the angular distributions for the ^{58}Ni + ^{12}C reaction at eight bombarding energies. The statistical errors are smaller than the symbols. The solid lines represent the best fit to the experimental data (see text). The values for ℓ_{max} shown are the maximum angular momenta used in the fitting.

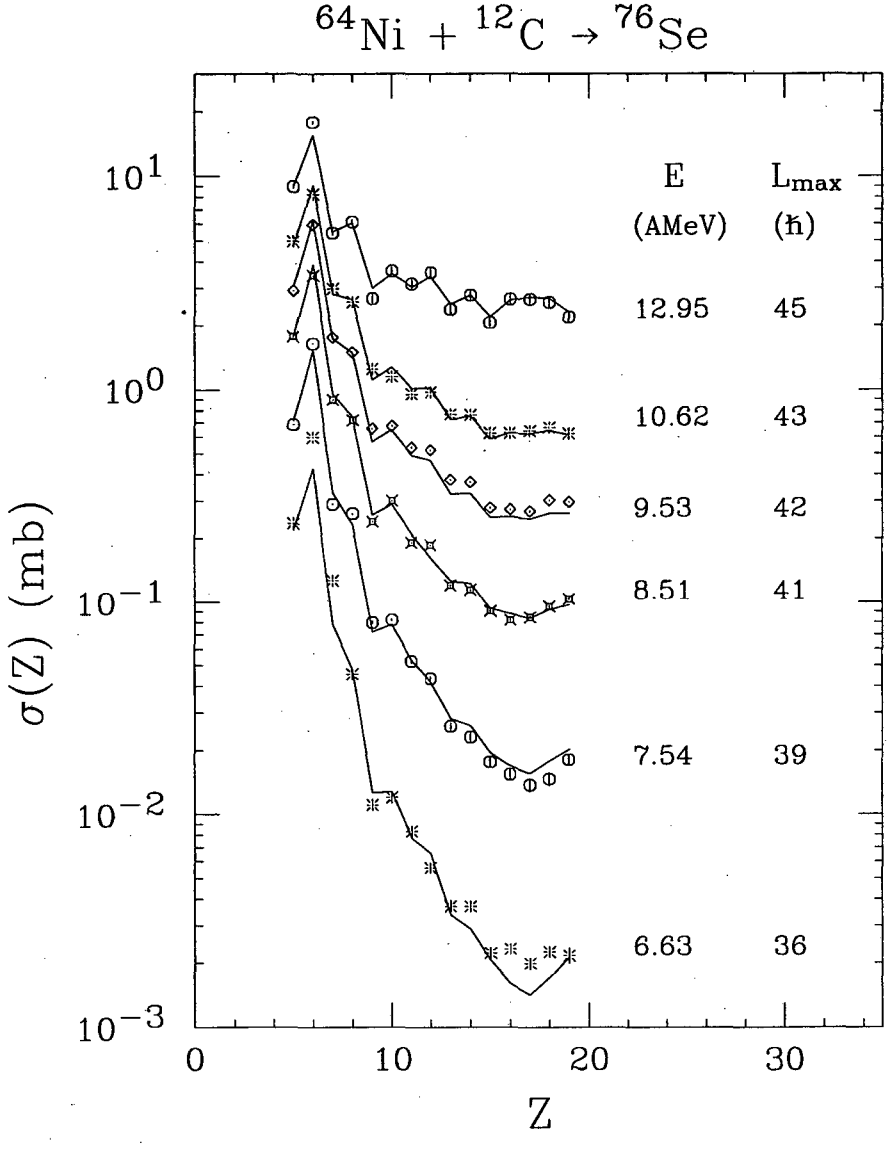

FIG. 6: Same as in Fig. 5 for the ^{64}Ni + ^{12}C reaction at six bombarding energies.

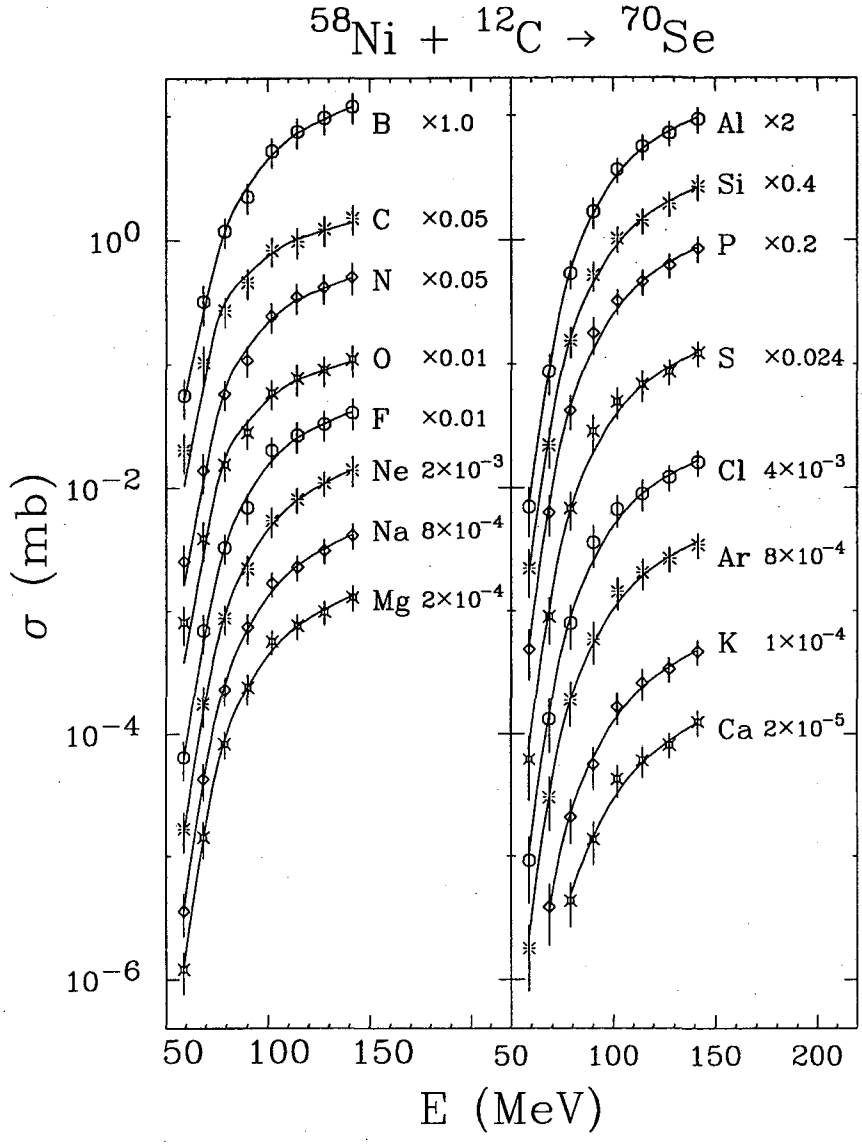

FIG. 7: The excitation functions for emission of complex fragments from the compound nucleus ^{70}Se produced in the ^{58}Ni + ^{12}C reaction. The error bar on each point corresponds to the sum of the systematic and statistical errors. The curves are the fitting results (see the text of Section IV). The number to the right indicates the factor by which each curve and the set of experimental data was multiplied for visual clarity.

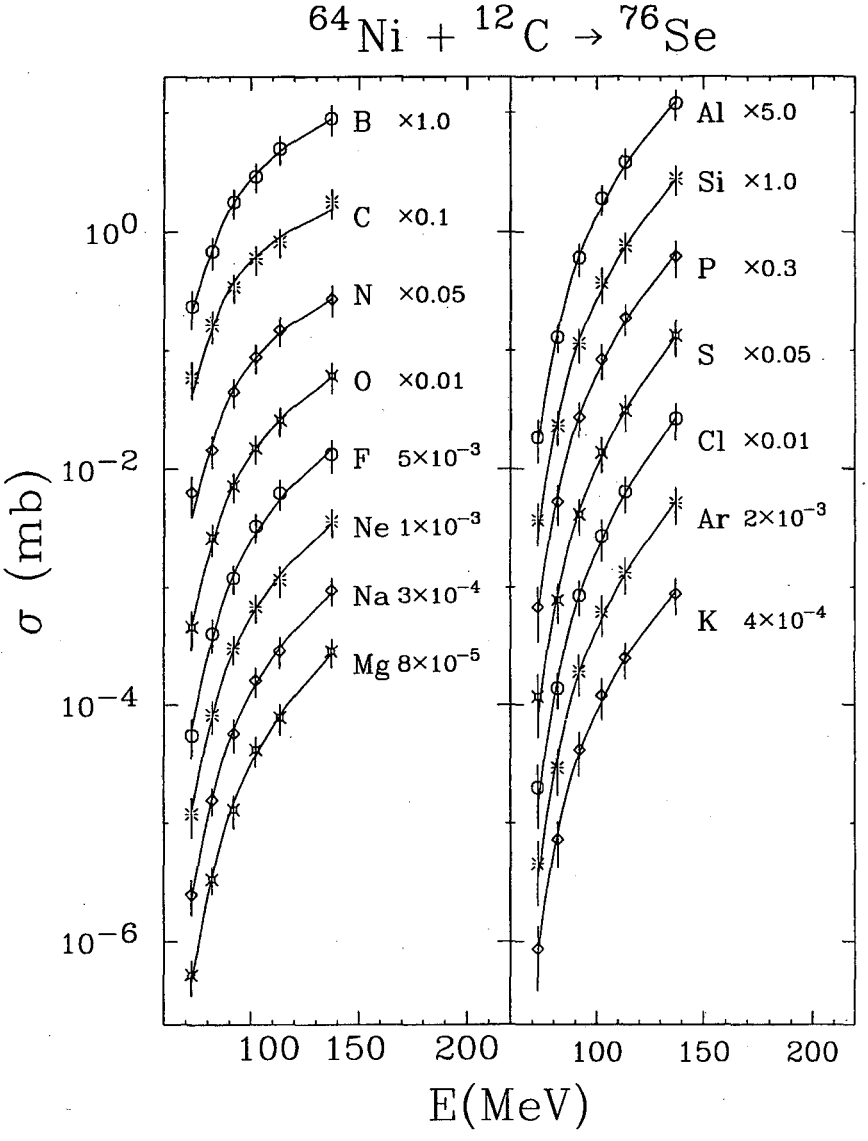

FIG. 8: Same as in Fig. 7 for the compound nucleus ^{76}Se produced in the ^{64}Ni + ^{12}C reaction.

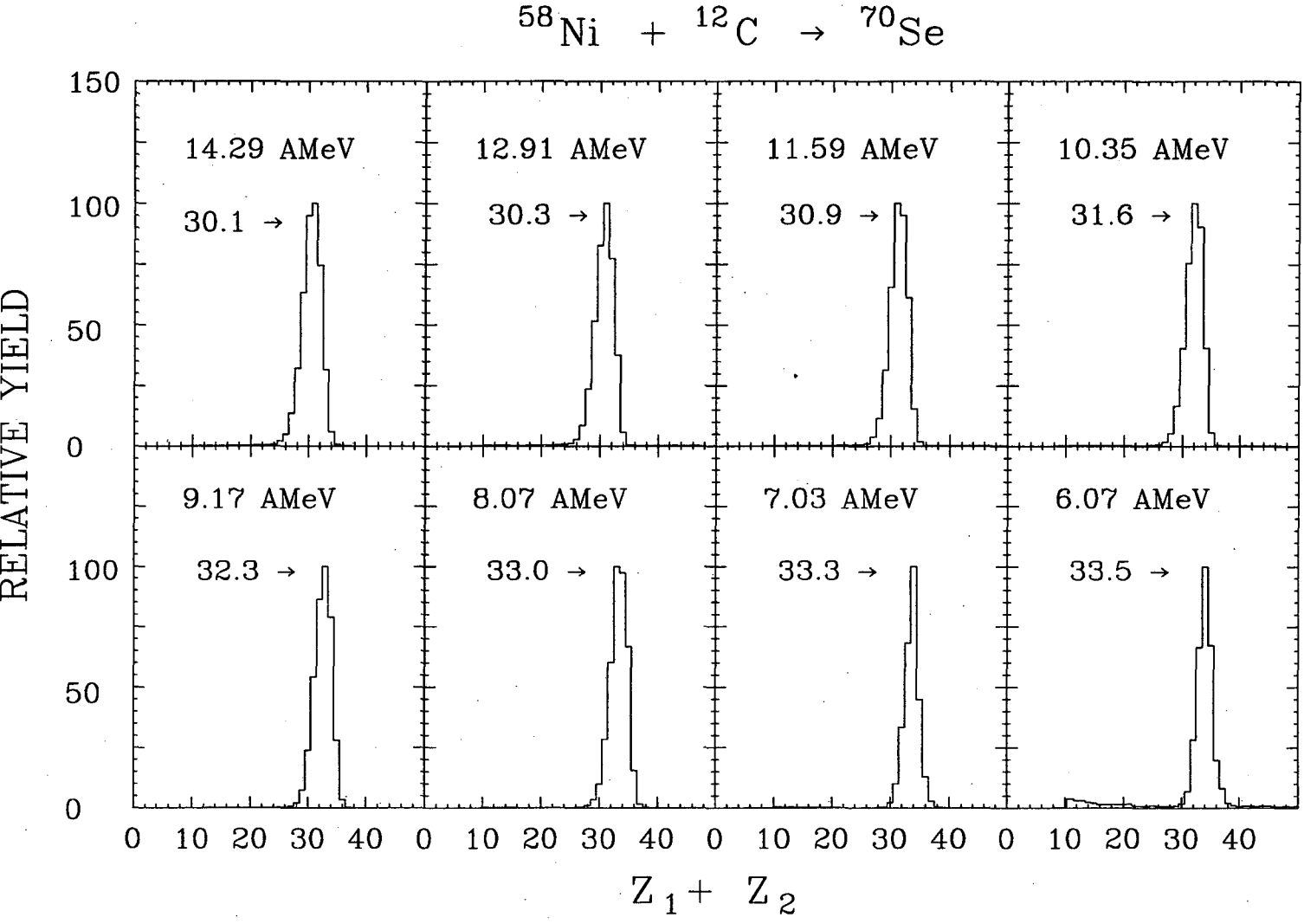

FIG. 9: The relative yield of coincidence events plotted as a function of the total charge of two coincident fragments for the $^{58}Ni + ^{12}C$ reaction at eight bombarding energies. For each bombarding energy, the mean total detected charge is indicated.

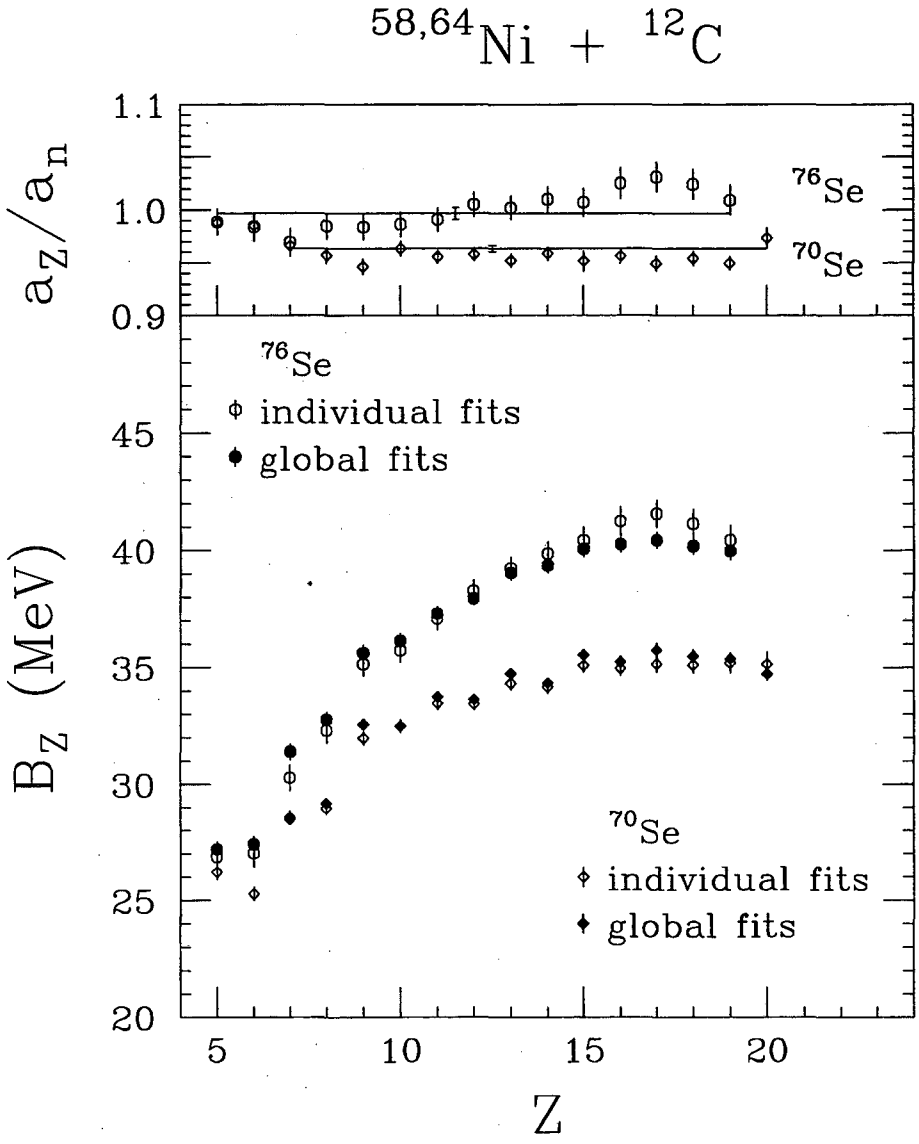

FIG. 10: The experimental mass-asymmetric barriers (B_Z) and the ratio of the level density parameters (a_Z/a_n) for the compound nuclei ^{70}Se and ^{76}Se, extracted from fitting the excitation functions. The open symbols are obtained by the individual fits. The error bars shown are the standard errors arising solely from the uncertainties of the cross sections. The filled symbols and solid lines are obtained from the global fits. The error bars shown for global fitting take into account the uncertainties of the cross sections and both parameter correlations and non-linearities. The uncertainties arising from choice of these parameters are discussed in the text and not included in the errors bars.

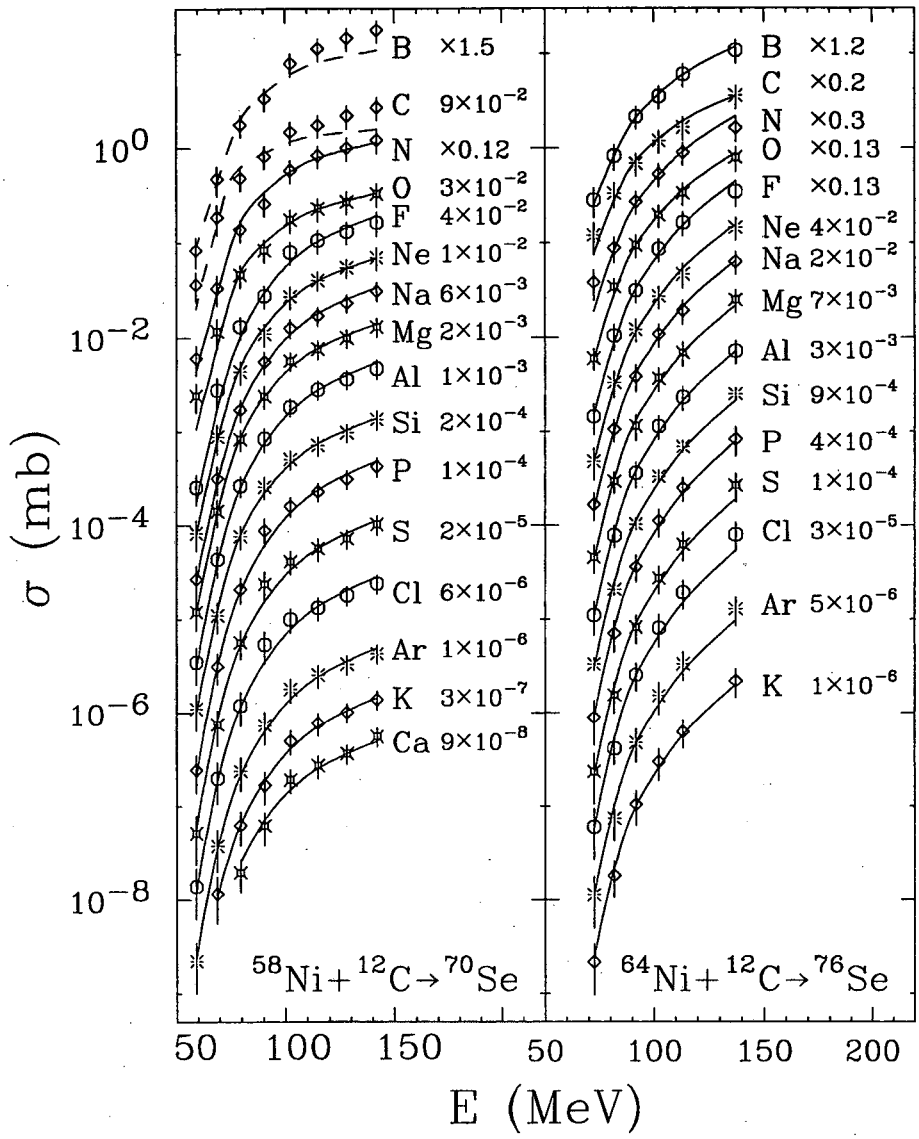

FIG. 11: The excitation functions for emission of complex fragments from the compound nuclei ^{70,76}Se. The curves are the global fitting results (see the text of Section IV). The number to the right indicates the factor by which each curve and the set of experimental data was multiplied for visual clarity.

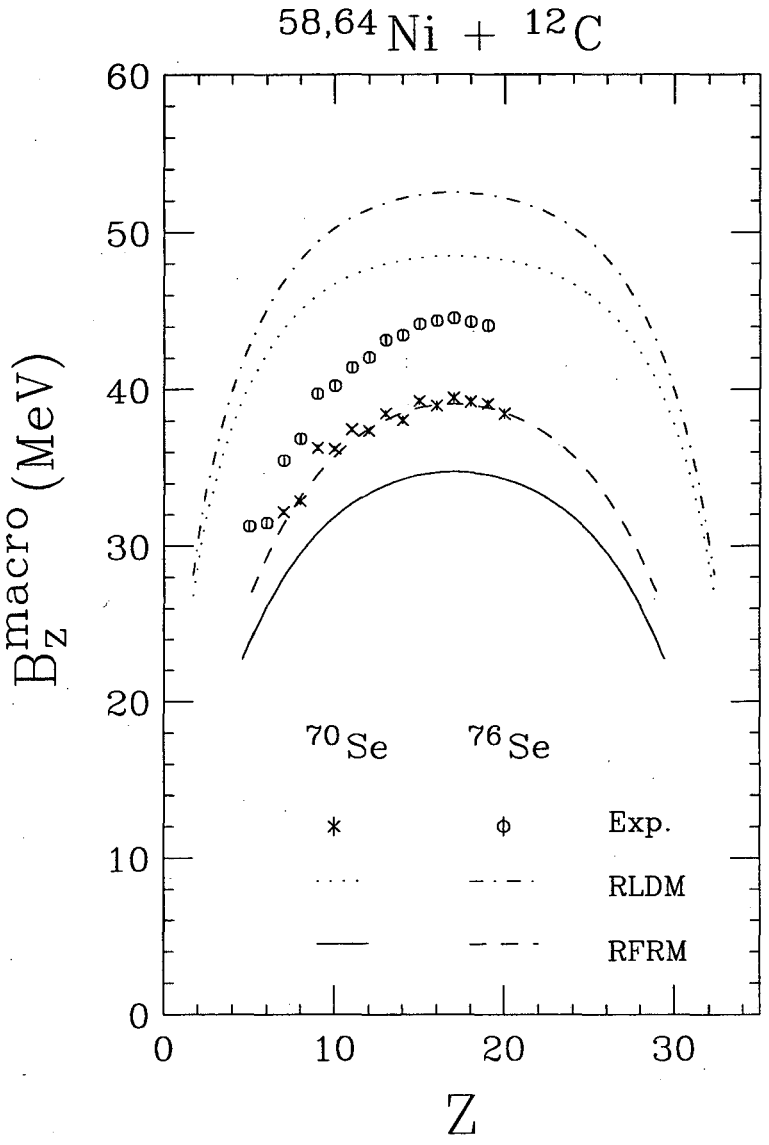

FIG. 12: Experimental mass-asymmetric fission barriers (symbols)corrected for shell effects are compared to Rotating Liquid Drop Model (RLDM) and Rotating Finite Range Model (RFRM) calculations for the compound nuclei ^{70,76}Se.

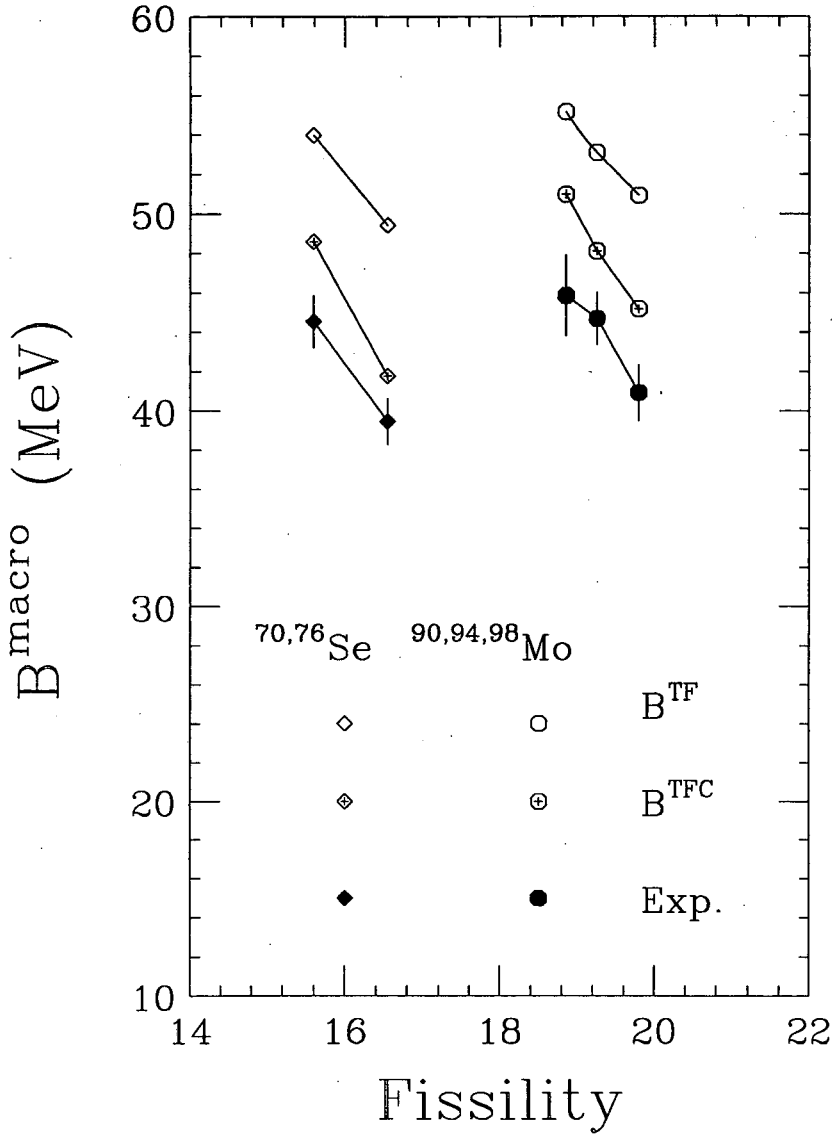

FIG. 13: Measured symmetric fission barriers corrected for ground-state shell effects and the Thomas-Fermi Model calculations are plotted against the fissility parameter which is definded as $Z^2/A(1-2.2I^2)$ where $I=(N-Z)/A$. The filled symbols are the measured macroscopic symmetric fission barriers for the compound nuclei ^{70,76}Se, ^{90,94,98}Mo [7], respectively. The errors shown are the total errors. The open symbols (B^{TF}) assume that the congruence energy at the saddle point is the same as in the ground state. The symbols filled with crosses (B^{TFC}) take into account the shape dependence of the congruence energy.

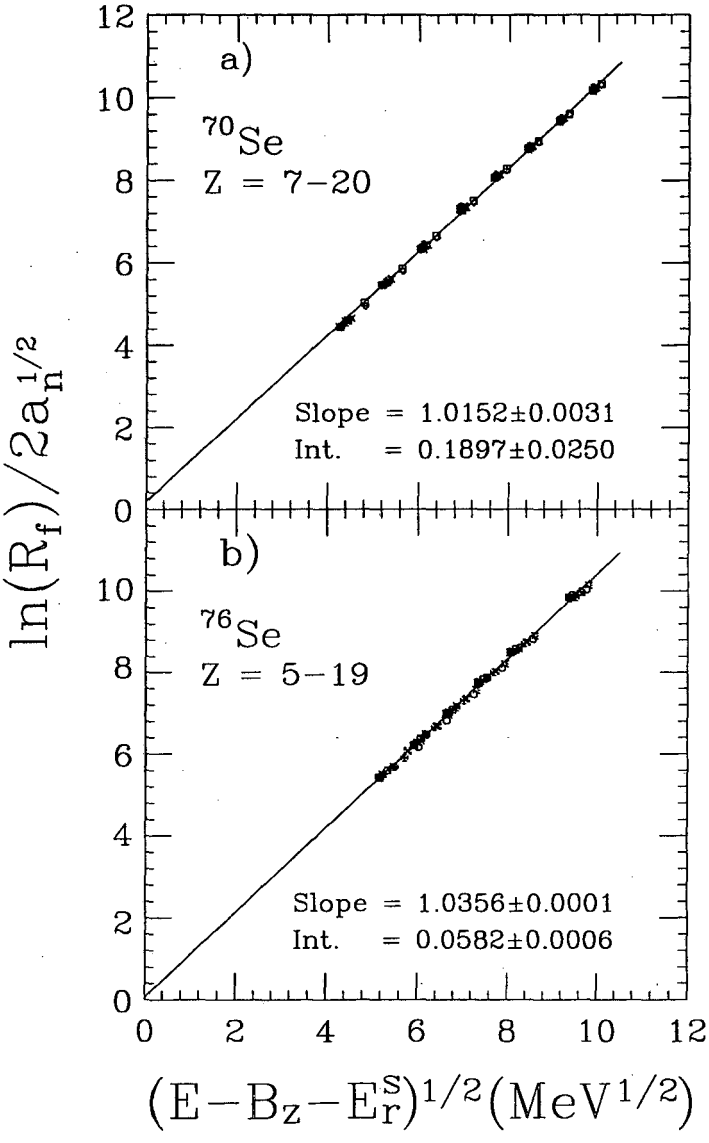

FIG. 14: The logarithm of the reduced fission rate R_f as defined in Eq. 9 divided by $2\sqrt{a_n}$ versus the square root of the internal excitation energy over the saddle-point for the compound nuclei ^{70,76}Se. The solid lines are linear fits to the data.

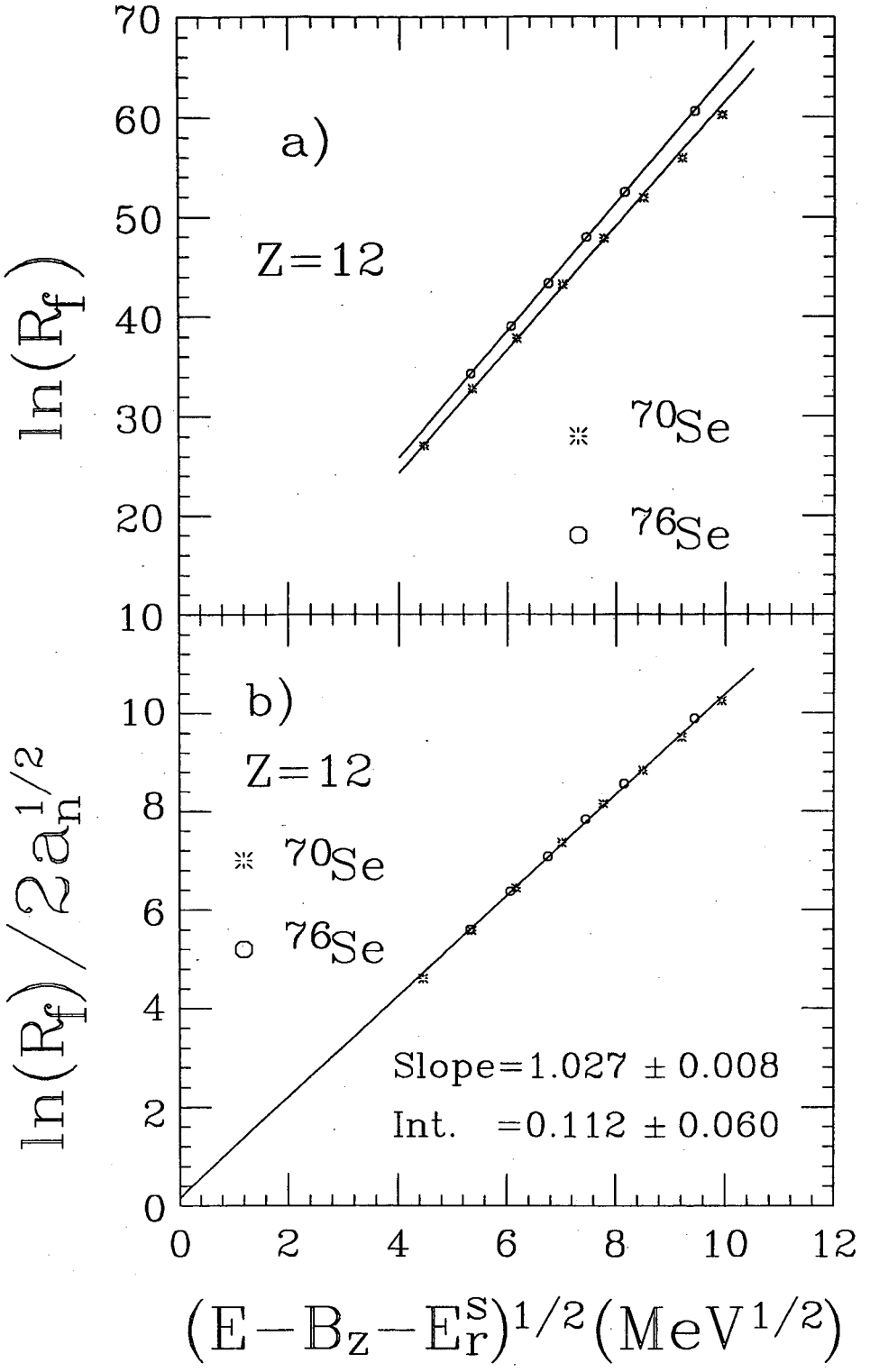

FIG. 15: (a) The quantities $\ln R_f$ and (b) $\ln R_f$ divided by $2\sqrt{a_n}$ versus the square root of the internal excitation energy for fragments $Z = 12$ emitted from the compound nuclei ^{70,76}Se. The solid lines are linear fits to the data.

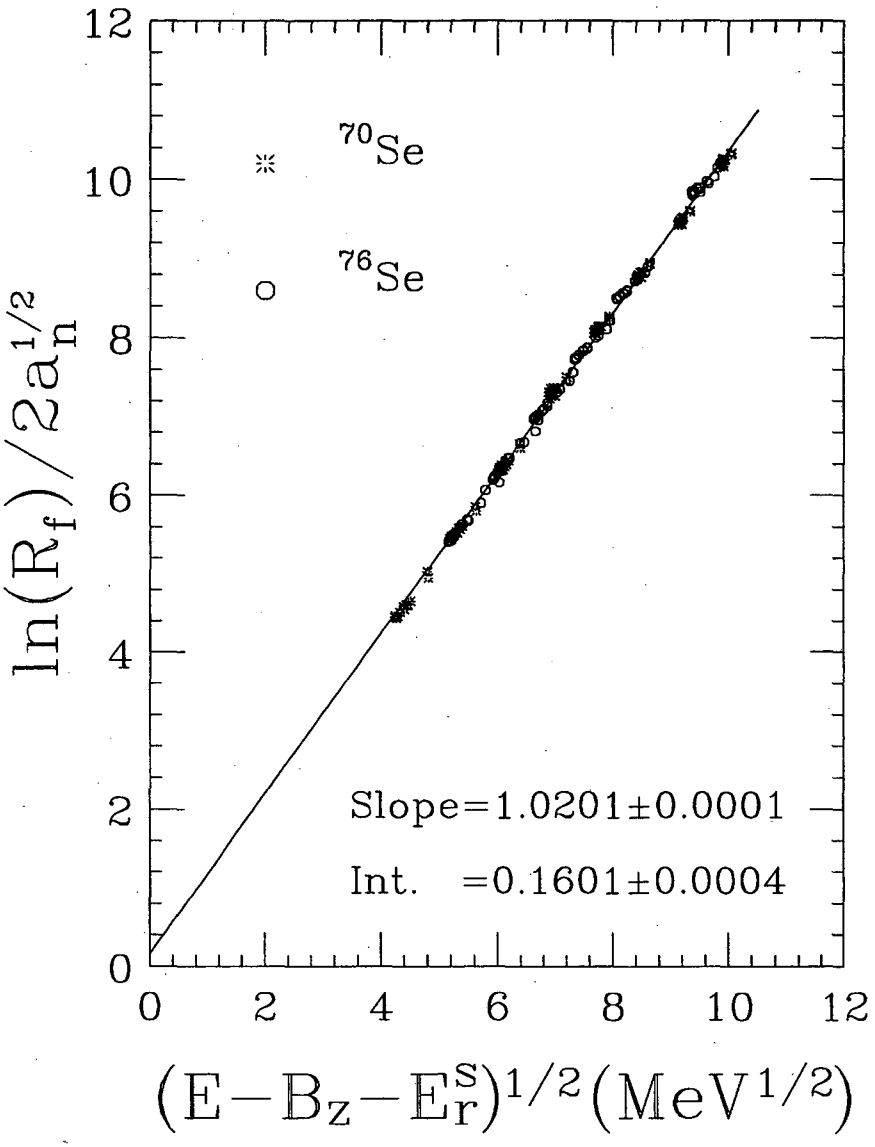

FIG. 16: Same as Figs. 14 & 15(b) with the data for all Z values from the two compound nuclei shown in a single plot. The straight line is the linear fit to all the data points.

Ernest Orlando Lawrence Berkeley National Laboratory
One Cyclotron Road | Berkeley, California 94720

Prepared for the U.S. Department of Energy under Contract No. DE-AC03-76SF00098